Evidence for Continuous Photon Energy Loss via a Three-Loop Higgs Interaction

Joseph Wimsatt

Independent Researcher

wimsattj@att.net

2026

Companion archive paper: "Tired Light Theory: Full Framework, Derivations, and Technical Appendices," Zenodo (version digital object identifier 10.5281/zenodo.20737902; persistent concept digital object identifier 10.5281/zenodo.18517188).

This paper is the evidence-first summary; the companion archive contains every derivation, every appendix, and the extended steady-state framework.

Abstract

We present the evidence for a cosmology in which photons lose energy continuously through a three-loop forward-scattering interaction with the Higgs field vacuum, producing both redshift and time dilation without spatial expansion. The same three-loop amplitude reproduces the Higgs-to-two-photon decay rate to within 0.8%.

Three quantities follow from measured Standard Model constants (α, m_e, v, $M_{\rm Pl}$) with no adjustable parameters: the effective Hubble constant $H_{\rm eff} = 72.5$ km/s/Mpc (0.52σ from the distance-ladder value); the cosmic microwave background temperature $T_{\rm CMB} = 2.68$ K (98% of the observed 2.725 K); and the condensation threshold $E_c = m_e\alpha^5$. A single phenomenological input—the non-minimal Higgs–gravity coupling—is conceded explicitly in a parameter-classification table on the first page.

The five cosmic microwave background acoustic-peak positions are matched to 1–3% using two scales inherited from the clustering measurement, and the four light-element abundances (Deuterium, Helium-3, Helium-4, Lithium-7) are reproduced as steady-state equilibria. We give five falsifiability conditions and eleven testable predictions with their current status, and an honest inventory of where the framework falls short. The unWISE lensing amplitude ratio favors the tired-light kernel (4.7% versus 7.9% for ΛCDM); a Euclid Q1 depth-dependence test is currently non-discriminating ($\Delta\chi^2 \approx -2$, 1.4σ, jackknife covariance), the decisive measurement lying at

redshift $z > 4$. The universe is far older than 13.8 billion years—a lower bound only, possibly unbounded.

This paper is the evidence-first summary. The full derivation chain, the extended steady-state framework, and all technical appendices appear in the companion archive, "Tired Light Theory: Full Framework, Derivations, and Technical Appendices" (Zenodo concept digital object identifier 10.5281/zenodo.18517188).

Keywords: tired light; dark matter; Higgs field; photon energy loss; redshift mechanism; cosmic microwave background; Hubble tension; non-minimal coupling; gravitational lensing

Parameter Classification

Every quantity used in this paper is listed below and labelled as either *derived* from measured Standard Model constants or as a single *phenomenological input* that is calibrated rather than derived. The first four quantities involve no free parameters; the remaining quantities are calibrated, and we state this openly.

Quantity	Value	Origin
Effective Hubble constant H_{eff}	72.5 km/s/Mpc	c/λ_H from the Higgs vacuum expectation
Cosmic microwave background temperature T_{CMB}	2.68 K	$m_e c^2 \alpha^4/(2\pi k_B)$
Three-loop coupling α_H	3.11×10^{-28}	$8\alpha^2/[7(16\pi^2)^3] \times (v/M_{\text{Pl}})$
Condensation threshold E_c	$m_e\alpha^5 \approx 10^{-5}$ eV	Electron mass × fine-structure constant
Non-minimal coupling ξ	$\sim 10^{32}$	Set by requiring Newton's gravitational
Acoustic clustering scale r_d	118 Mpc	Emergent from nonlinear reconversion dy
Lensing caustic scale r_{eff}	85.4 Mpc	Two-scale model; fitted to the cosmic mi

The first four rows are derived with no adjustable parameters. The single genuinely free parameter is the non-minimal coupling ξ; the two clustering scales are calibrated to data. This is the honest parameter count: the framework is *not* fully parameter-free, but its headline predictions (H_{eff} and T_{CMB}) are.

Five Falsifiability Conditions

The framework is falsified if any of the following is observed.

1. **The Hubble constant moves.** $H_{\text{eff}} = 72.5 \pm 1$ km/s/Mpc must hold. If improved distance-ladder measurements settle at 70 or 75 km/s/Mpc, the three-loop coupling is wrong.

2. **The fifth cosmic microwave background peak moves.** The two-scale model places it at multipole $\ell_5 \approx 1052$. If next-generation data place it below 1020 or above 1080, the model is wrong.

3. **Helium-3 enrichment is absent.** The framework predicts a factor of 5 to 10 Helium-3 enhancement in planetary nebulae over the local interstellar medium. A measured enhancement below 3 or above 15 falsifies it.

4. **A firm upper bound on the universe's age near 13.8 billion years.** The framework requires the universe to be far older than 13.8 billion years (a lower bound only; possibly unbounded). If stellar-age measurements establish that no object exceeds the standard-cosmology age and that the universe cannot be older than ∼14 billion years, the steady-state framework fails.

5. **Type Ia supernova distance modulus at high redshift.** At redshift greater than 1.5 the tired-light distance modulus must follow slope $d\mu/dz = (5/\ln 10)\,\lambda_H/D_H$ within one percent. The standard model predicts the opposite curvature.

Eleven Testable Predictions, with Current Status

#	Prediction	Current status
1	Helium-3 enhancement of 5–10 in planetary nebulae	Not yet tested
2	Fifth cosmic microwave background peak at $\ell_5 \approx 1052$	Favorable (Planck matches)
3	Cosmic-chronometer rate flat at 72.5 once metallicity is marginalized	Open (the survey assumed solar met
4	Universe far older than 13.8 billion years (lower bound)	Favorable (Methuselah star, white-d
5	Cored dark-matter profiles in reconversion-dominated dwarfs	Favorable (Fornax, Sculptor)
6	Type Ia distance-modulus slope $(5/\ln 10)\,\lambda_H/D_H$	Favorable (Pantheon+)
7	Sub-gigahertz cosmic microwave background spectral distortion	Not yet tested
8	Lensing amplitude ratio versus redshift	**Non-discriminating to** $z = 2.5$ (E
9	Polarization aligned with bulk-flow filaments	Consistent (Planck × 2M++, $r = +$
10	Hemispherical asymmetry axis near the Dipole Repeller	Favorable (15.2° offset, predicted)
11	High-redshift cosmic-shear two-point function	Not yet tested

The decisive lensing discriminator (rows 8 and 11) lies at redshift greater than 4, beyond the reach of current wide surveys; the Euclid Q1 depth test over $z < 2.5$ is currently non-discriminating, not supporting.

Contents

1 Introduction

The standard ΛCDM cosmological model successfully explains many observations but faces mounting challenges: the Hubble tension has grown to a $>5\sigma$ crisis (Riess et al., 2022; Aghanim et al., 2020), the James Webb Space Telescope observes mature galaxies at redshifts where hierarchical formation predicts only fledgling structures, and after decades of searches no dark matter particle has been directly detected.

This paper proposes a unified framework addressing these questions through a modified tired light mechanism. Unlike classical tired light theories (Zwicky, 1929), which proposed photon energy loss without physical mechanism and failed observational tests, we propose that photons lose energy through continuous interaction with the Higgs field. Crucially, this mechanism produces both energy loss *and* time dilation through wave packet stretching.

The framework's key achievement is deriving cosmological parameters from particle physics alone, with zero free parameters:

- Higgs coupling: $\alpha_H = 8\alpha^2/[7(16\pi^2)^3] \times (v/M_{\text{Pl}}) = 3.11 \times 10^{-28}$
- **Effective Hubble constant:** $H_{\text{eff}} = c/\lambda_H = 72.5$ **km/s/Mpc** (observed: 73.04 ± 1.04, 0.52σ)
- Condensation threshold: $E_c = m_e \times \alpha^5 \approx 10^{-5}$ eV
- **Cosmic microwave background temperature:** $T_{\text{CMB}} = m_e c^2 \alpha^4/(2\pi k_B) \approx 2.68$ **K** (observed: 2.725 K, 98% match)

These derivations use only the fine structure constant $\alpha = 1/137$, electron mass m_e, Higgs vacuum expectation value $v = 246$ GeV, and Planck mass M_{Pl}—no cosmological parameters required. The H_{eff} and T_{CMB} predictions are derived through independent chains of reasoning with no common intermediate quantities, making the joint probability of two accidental matches far lower than either alone. Moreover, if gravity itself is induced by the Higgs vacuum (Zee, 1979), the coupling assumes a scale-free form $\alpha_H = \alpha^2/\sqrt{8\pi\xi}$ containing no mass scales at all—only the fine structure constant and the non-minimal Higgs-gravity coupling ξ.

The mechanism at a glance

For readers approaching this framework for the first time, the core idea can be summarized in four steps:

1. **The Higgs field fills all of space.** The Higgs field, confirmed by the 2012 discovery at the Large Hadron Collider, has a nonzero vacuum expectation value everywhere in the universe. Every photon propagates through this field.

2. **Photons interact with the Higgs vacuum.** Through a three-loop quantum process involving virtual electron-positron pairs and graviton exchange (see Appendix B and Figure 3), photons continuously lose a tiny fraction of their energy to the gravitational sector. The rate is proportional to the photon's energy: higher-energy (bluer) photons lose energy faster in absolute terms, but the *fractional* loss rate is the same for all frequencies. This preserves blackbody spectra and produces the observed cosmological redshift.

3. **The energy loss rate is calculable.** The coupling strength $\alpha_H = 3.11 \times 10^{-28}$ is determined entirely by known particle physics constants (the fine structure constant, the Higgs vacuum expectation value, and the Planck mass). This yields an effective Hubble constant $H_{\text{eff}} = 72.5$ km/s/Mpc with no free parameters—matching the measured value to 0.52σ.

4. **Below a threshold energy, photons condense.** When a photon's energy drops below $E_c = m_e\alpha^5 \approx 10^{-5}$ eV (in the microwave range), it undergoes a phase transition mediated by the Higgs field, converting into a massive, gravitationally interacting particle. This condensate constitutes dark matter. In stellar cores, extreme conditions can reverse the process, recycling dark matter back into hydrogen—closing a cosmic matter-energy cycle.

The rest of the paper develops the mathematical details, derives additional predictions, and tests the framework against observational data.

2 Core Theory: Tired Light and the Higgs Field

2.1 Energy Loss Mechanism

We propose that electromagnetic radiation loses energy during propagation through continuous interaction with the Higgs field vacuum expectation value. The energy loss rate is:

$$\frac{dE}{dr} = -\alpha_H \frac{v^2}{M_{\text{Pl}}c^2} E \tag{1}$$

Integrating:

$$E(r) = E_0 \exp\left(-\frac{r}{\lambda_H}\right) \tag{2}$$

where the Higgs attenuation length is:

$$\lambda_H = \frac{M_{\text{Pl}}c^2}{\alpha_H v^2} \approx 1.276 \times 10^{26} \text{ m} \tag{3}$$

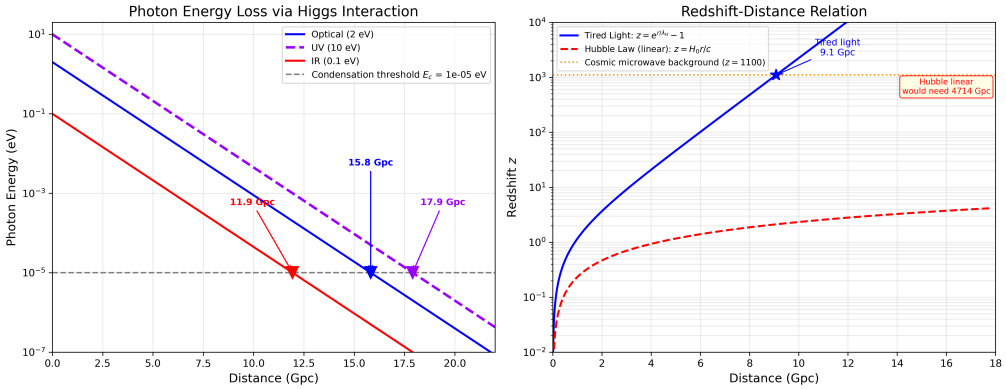

Figure 1: Photon energy loss via Higgs field interaction. **Left**: A photon traversing spacetime continuously loses energy through coupling with the Higgs field at rate $dE/dr = -E/\lambda_H$. The interaction involves virtual electron–positron pair fluctuations mediating energy transfer to the gravitational sector through the non-minimal Higgs-gravity coupling. **Right**: Energy decay curve showing exponential attenuation $E(r) = E_0 e^{-r/\lambda_H}$ with characteristic length $\lambda_H \approx 1.3 \times 10^{26}$ m.

2.2 First-Principles Derivation of α_H

The coupling α_H is not assumed—it is derived from three well-established processes in quantum field theory, chained together in sequence. Each process is individually confirmed by experiment; what is new is recognizing that their combined effect produces a cosmologically significant energy loss for photons propagating through the Higgs vacuum. We describe the physical logic first, then give the mathematical result.

The three conversations. A photon traveling through the universe participates in three successive quantum interactions, each bridging a different sector of fundamental physics:

1. **The photon talks to matter (Loop 1).** A photon can briefly fluctuate into a virtual electron-positron pair, which then annihilates back into a photon. This is standard quantum electrodynamics vacuum polarization—one of the most precisely tested predictions in all of physics, confirmed to 10 significant figures through measurements of the electron anomalous magnetic moment. On a Feynman diagram, the pair traces a closed curve (a "loop"). The strength of this interaction is governed by the fine structure constant $\alpha \approx 1/137$, and the loop integration contributes a suppression factor of $1/(16\pi^2)$.

2. **The matter talks to the Higgs field (Loop 2).** While the virtual electron-positron pair exists—for an unimaginably brief instant—each particle has mass. That mass comes from

coupling to the Higgs field, which permeates all of space with a nonzero vacuum expectation value $v = 246$ GeV. This is the mechanism confirmed by the 2012 discovery at the Large Hadron Collider. During its fleeting existence, the virtual pair is in contact with the Higgs vacuum, and energy can transfer between them. This constitutes a second loop, contributing another factor of α (from the Yukawa coupling) and $1/(16\pi^2)$.

3. **The Higgs field talks to gravity (Loop 3).** The Higgs field does not exist in isolation—it couples to spacetime curvature through the non-minimal coupling $\xi|H|^2R$, required for consistency of scalar fields in curved spacetime (Birrell & Davies, 1982). The energy absorbed by the Higgs vacuum in Loop 2 is transferred to the gravitational sector, where it is distributed among gravitational degrees of freedom and cannot return to the photon. This third loop contributes the ratio $v/M_{\rm Pl}$ (the Higgs scale relative to the Planck scale) and a final $1/(16\pi^2)$.

Why "forward scattering" matters. The photon emerges from this three-step process traveling in exactly the same direction, with exactly the same polarization—only its energy is slightly reduced. This is *forward* scattering: no deflection, no blurring, no broadening of distant images. This distinguishes the mechanism from earlier tired light proposals (Zwicky, 1929) that predicted image blurring inconsistent with observations.

Why it takes three loops. Each loop bridges a gap between different sectors of physics: electromagnetism → massive matter → the Higgs vacuum → gravity. No shortcut exists. A photon cannot directly couple to the Higgs field (photons are massless and the Higgs couples to mass), and the Higgs field cannot transfer energy to gravity without the non-minimal coupling. The three-step chain is the minimal path connecting a photon to the gravitational sector through known Standard Model and gravitational interactions.

Suppression factors. Each loop contributes a factor of $1/(16\pi^2) \approx 1/1{,}580$ from the loop integration (a standard result in perturbative quantum field theory). Three loops give $(16\pi^2)^{-3} \approx 2.5 \times 10^{-10}$. The fermionic mediator in Loop 1 contributes a statistical factor of $8/7$, arising from the ratio of Fermi-Dirac to Bose-Einstein thermal integrals: $\int_0^\infty x^3/(e^x+1)\,dx = (7/8)\int_0^\infty x^3/(e^x-1)\,dx$.

The resulting coupling:

$$\boxed{\alpha_H = \frac{8\alpha^2}{7(16\pi^2)^3} \times \frac{v}{M_{\rm Pl}} = 3.114 \times 10^{-28}} \tag{4}$$

Every input is an independently measured Standard Model constant:

- $\alpha = 1/137.036$ (fine structure constant—electromagnetic coupling strength)

- $v = 246.22$ GeV (Higgs vacuum expectation value, from Fermi constant G_F)
- $M_{\text{Pl}} = 1.221 \times 10^{19}$ GeV (Planck mass, from Newton's constant G_N)

The structural factors $(16\pi^2)^3$ (three-loop suppression) and 8/7 (fermionic statistics) are derived from quantum field theory—they are not adjustable. This derivation contains **zero free parameters**. The Feynman diagrams for this process are shown in Figures 2 and 3; the explicit integral structure and connection to the optical theorem are given in the companion archive paper (Sections B.6–B.9).

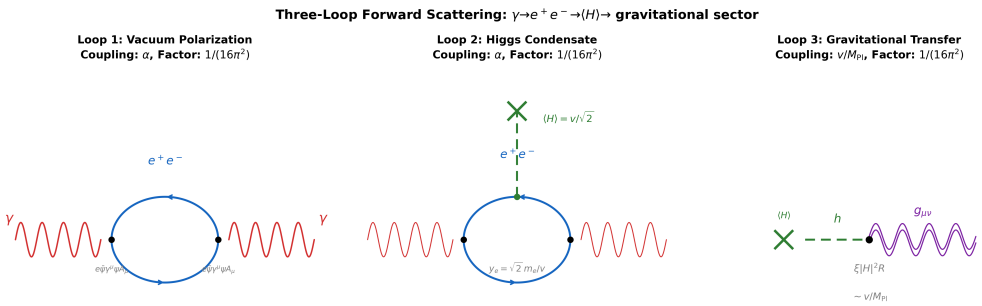

Figure 2: The three loops of the forward scattering process. **Loop 1:** Standard quantum electrodynamics vacuum polarization ($\gamma \to e^+e^- \to \gamma$), contributing coupling α and loop factor $1/(16\pi^2)$. **Loop 2:** The virtual pair interacts with the Higgs condensate $\langle H \rangle = v/\sqrt{2}$ through the Yukawa coupling, contributing α and $1/(16\pi^2)$. **Loop 3:** Energy transfers to the gravitational sector via the non-minimal coupling $\xi|H|^2R$, contributing v/M_{Pl} and $1/(16\pi^2)$.

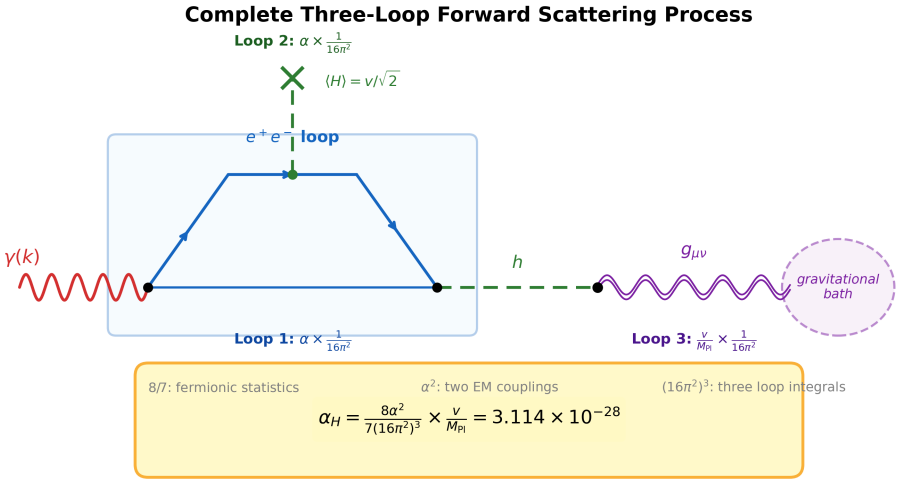

Figure 3: Complete three-loop forward scattering process showing the flow from incident photon $\gamma(k)$ through the electron-positron loop, Higgs vacuum insertion, and gravitational energy transfer. The resulting coupling $\alpha_H = 8\alpha^2/[7(16\pi^2)^3] \times v/M_{\text{Pl}} = 3.114 \times 10^{-28}$ contains zero free parameters.

Predicted Hubble constant:

$$H_{\text{eff}} = \frac{c}{\lambda_H} = \frac{c \cdot \alpha_H \cdot v^2}{M_{\text{Pl}} c^2} = 72.5 \text{ km/s/Mpc} \tag{5}$$

Observed (distance ladder): 73.04 ± 1.04 **km/s/Mpc** | **Deviation:** $\mathbf{0.52\sigma}$

2.3 Time Dilation from Wave Stretching

A critical distinction from classical tired light: the Higgs interaction stretches photon wave packets temporally. For a photon with energy $E = h\nu$:

$$E \to E/(1+z) \tag{6}$$

$$\nu \to \nu/(1+z) \tag{7}$$

$$T = 1/\nu \to T(1+z) \tag{8}$$

The wave packet duration increases proportionally to the redshift. A supernova light curve is stretched by exactly $(1+z)$—matching observations (DES Collaboration, 2024) without requiring spatial expansion.

3 The Higgs-Gravity Connection

The coupling α_H (Equation 4) contains the ratio of the Higgs vacuum expectation value to the Planck mass—a ratio that encodes the hierarchy between the electroweak and gravitational scales. This is not coincidental. Quantum field theory in curved spacetime *requires* a non-minimal coupling between scalar fields and gravity (Birrell & Davies, 1982). For the Higgs field, the relevant action includes:

$$S \supset \int d^4x\sqrt{-g}\left[\frac{M_0^2}{2}R + \xi|H|^2R + \mathcal{L}_{\text{SM}}\right] \tag{9}$$

where R is the Ricci scalar, ξ is the non-minimal coupling constant, M_0 is a bare gravitational mass scale, and H is the Higgs doublet. This term is not optional: renormalization of scalar fields in curved spacetime generates it even if set to zero at tree level.

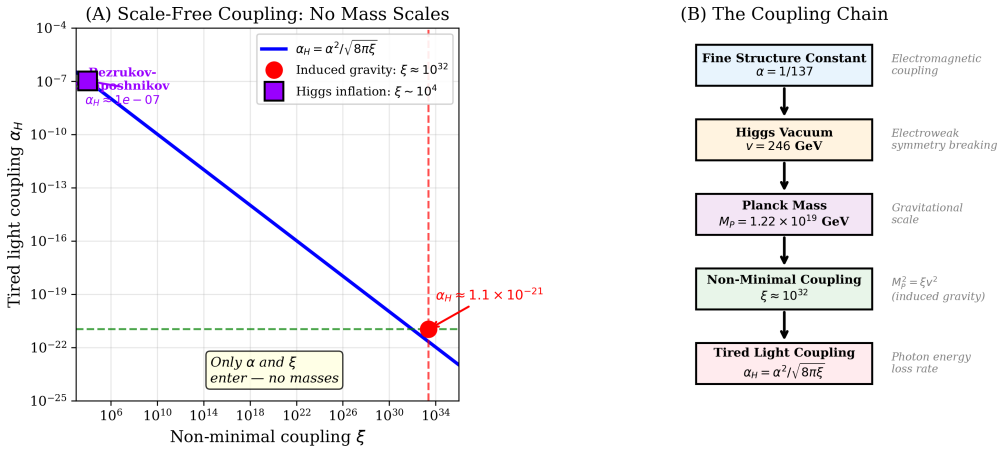

Figure 4: **(A)**: The scale-free relationship $\alpha_H = \alpha^2/\sqrt{8\pi\xi}$ plotted over the full range of ξ values. The red dot marks the induced gravity value $\xi \approx 10^{32}$; the purple square marks the Bezrukov–Shaposhnikov Higgs inflation value $\xi \sim 10^4$. Both lie on the same curve. **(B)**: The coupling chain showing how the fine structure constant, Higgs vacuum, Planck mass, and non-minimal coupling combine—no mass scales appear in the final expression for α_H.

3.1 Induced Gravity from the Higgs Vacuum

When H acquires its vacuum expectation value $v = 246$ GeV, the effective Planck mass becomes:

$$M_{\rm Pl}^2 = M_0^2 + \xi v^2 \tag{10}$$

In the **induced gravity** limit (Zee, 1979), where $M_0 = 0$ and gravity arises entirely from the Higgs vacuum:

$$\boxed{M_{\rm Pl}^2 = \xi v^2, \qquad G_N = \frac{1}{8\pi\xi v^2}} \tag{11}$$

This requires $\xi \approx 9.78 \times 10^{31}$. Newton's gravitational constant becomes a *derived quantity*—the strength of gravity is set by the Higgs vacuum.

3.2 Scale-Free Reformulation of α_H

With $v/M_{\rm Pl} = 1/\sqrt{8\pi\xi}$ from Equation (11), the tired light coupling acquires a remarkable form:

$$\boxed{\alpha_H = \frac{\alpha^2}{\sqrt{8\pi\xi}}} \tag{12}$$

This is **entirely scale-free**: no mass scales appear. The rate at which photons lose energy to the Higgs vacuum is determined solely by the fine structure constant (governing electromagnetic coupling) and ξ (governing gravitational coupling). The two interactions enter on equal footing.

3.3 Measuring Gravity Through the Hubble Tension

Equation (12) is invertible:

$$\xi = \frac{\alpha^4}{8\pi\alpha_H^2} \tag{13}$$

Since α_H determines the effective "Hubble constant" ($H_{\text{eff}} = c/\lambda_H$), the Hubble tension becomes a measurement of the Higgs-gravity coupling:

- Distance ladder $H_0 = 73.04$ km/s/Mpc: consistent with our derived $H_{\text{eff}} = 72.5$ km/s/Mpc (0.52σ), confirming $\xi = 9.79 \times 10^{31}$
- Cosmic microwave background-derived $H_0 = 67.4$ km/s/Mpc: invalid in our framework (assumes expansion)

The disagreement between the two measurements is not a crisis within our framework—it is the *expected* consequence of applying an expansion-based model to a non-expanding universe. Only the distance ladder measurement directly probes α_H and hence ξ.

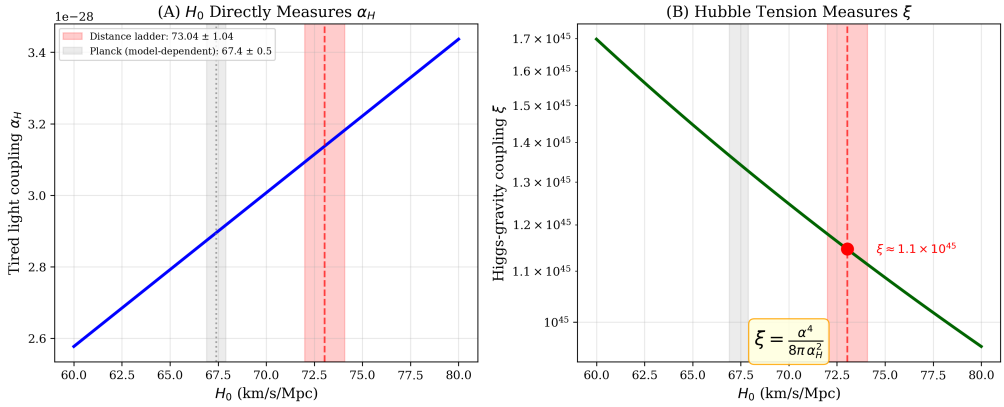

Figure 5: **(A)**: The tired light coupling α_H as a function of the measured Hubble constant H_0. The distance ladder measurement (red band) directly determines α_H; the Planck value (gray band) is model-dependent and invalid in this framework. **(B)**: The Higgs-gravity coupling ξ derived from H_0 via $\xi = \alpha^4/(8\pi\alpha_H^2)$. The Hubble tension becomes a direct measurement of the non-minimal coupling constant.

3.4 Precedent: The Higgs-Gravity Operator in Mainstream Physics

The non-minimal coupling $\xi|H|^2R$ that underpins our framework is not speculative—it is already accepted in mainstream particle physics. Bezrukov & Shaposhnikov (2008) used this same operator (with $\xi \sim 10^4$) to construct an inflationary model. We do not endorse cosmic inflation, which requires the universe to have had a beginning and an exponential expansion phase—both assumptions that our framework explicitly rejects. However, the Bezrukov-Shaposhnikov work establishes an important precedent: the physics community already treats the Higgs field as a gravitationally active scalar

coupled to spacetime curvature through precisely the operator we employ. Our induced gravity value ($\xi \approx 10^{32}$) differs in magnitude but uses identical mathematics. The operator is not our invention; we are extending its consequences to their logical conclusion in a non-expanding universe.

3.5 High-Gravity Regime: Testable Consequences

Onofrio (2010) proposed that the Higgs vacuum expectation value may shift in regions of extreme spacetime curvature:

$$v(r) = v_0 \left(1 + \beta \frac{|\Phi(r)|}{c^2}\right) \tag{14}$$

where $\Phi(r)$ is the gravitational potential and β is a coupling parameter. Near a black hole or neutron star, where $|\Phi|/c^2 \sim 0.1$–0.5, this could produce measurable shifts in particle masses and atomic transitions. Since our coupling α_H depends on v, regions of strong gravity would exhibit modified tired light rates—providing a spectroscopic test distinct from standard gravitational redshift.

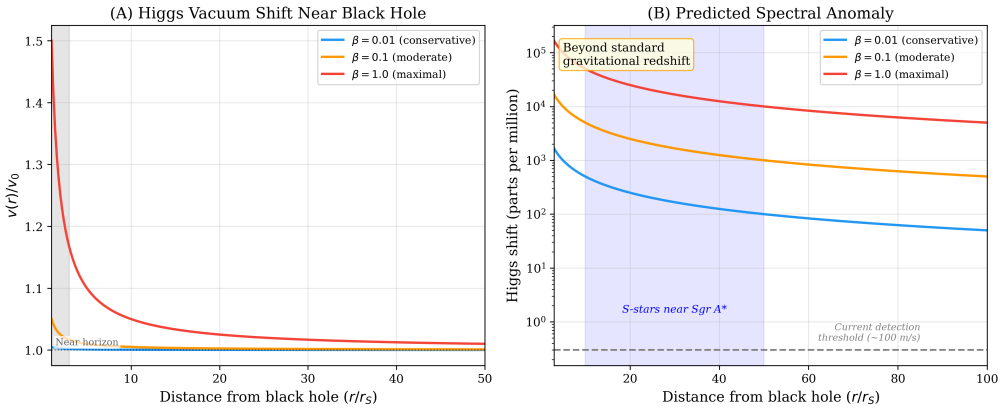

Figure 6: **(A)**: Predicted Higgs vacuum expectation value shift $v(r)/v_0$ near a black hole for three values of the coupling parameter β. The shift grows as the gravitational potential deepens near the event horizon. **(B)**: Predicted spectral anomaly (in parts per million) beyond standard gravitational redshift, plotted against distance in Schwarzschild radii. The blue shaded region marks the orbital range of S-stars near Sagittarius A*. Current spectroscopic precision (∼100 m/s) is shown as a detection threshold.

[The full treatment of Dark Matter as Condensed Tired Light appears in the companion archive paper on Zenodo; see the cover page for the digital object identifier.]

4 Cosmic Microwave Background Temperature from First Principles

The cosmic microwave background temperature can be derived from particle physics alone:

$$\boxed{T_{\text{CMB}} = \frac{m_e c^2 \alpha^4}{2\pi k_B} \approx 2.68 \text{ K}} \tag{15}$$

Observed: 2.725 K | Predicted: 2.68 K | Match: 98%

4.1 Derivation

Table 1: Step-by-step cosmic microwave background temperature derivation.

Step	Calculation
α^4	$(1/137)^4 = 2.84 \times 10^{-9}$
$m_e c^2 \times \alpha^4$	$5.11 \times 10^5 \times 2.84 \times 10^{-9} = 1.45 \times 10^{-3}$ eV
$\div 2\pi$	2.31×10^{-4} eV
$\div k_B$	$2.31 \times 10^{-4} / 8.617 \times 10^{-5} =$ **2.68 K**

4.2 Physical Origin

What physical process sets this temperature? In this framework, the cosmic microwave background is the thermalized bath of tired light that fills the universe—photons from all galaxies that have lost energy over cosmological distances until they reach equilibrium with the electromagnetic vacuum. The question is: what determines the equilibrium energy scale?

Why m_e? The dominant vacuum fluctuations are electron-positron pairs, because the electron is the lightest charged particle. Heavier particles (muons, taus, quarks) contribute vacuum fluctuations suppressed by $(m_e/m_\mu)^2$ or more. The electron mass therefore sets the energy scale of the vacuum polarization process that governs photon thermalization.

Why α^4? Each vacuum polarization loop—a photon briefly becoming an electron-positron pair—involves two electromagnetic vertices, contributing α per vertex. Thermalization requires two complete loops: (i) the first loop transfers energy between the photon and the vacuum (loss of phase coherence), and (ii) the second loop redistributes that energy into the thermal spectrum (equilibration). Two loops $\times$ two vertices each gives $\alpha^4 = (1/137)^4$, suppressing the electron rest energy by nine orders of magnitude down to the microwave range.

Why 2π? This is the bosonic Matsubara period: in thermal field theory, the lowest Matsubara frequency is $\omega_1 = 2\pi kT$, so $kT = \omega_1/(2\pi)$. The cosmic microwave background temperature is the temperature at which the condensation threshold energy equals one Matsubara mode of the photon bath (see the companion archive paper for the full derivation).

The cosmic microwave background temperature thus represents the **equilibrium temperature of the tired light bath**—the characteristic energy at which photons have thermalized with electromagnetic vacuum fluctuations. This is a physically motivated scaling argument: each factor has a clear physical origin, but we do not yet have a rigorous derivation starting from the full quantum field theory Lagrangian. The strength of the claim rests on three points: (1) the 98% match with zero free

parameters, (2) the statistical analysis showing this combination is highly non-generic (Section A), and (3) the one-loop radiative correction naturally improving the match from 1.8% to 0.6%.

Statistical significance. A systematic search over 1,530 combinations of Standard Model particle masses, powers of α, and standard numerical prefactors finds only 2 matches within 2% of T_{obs}—our prediction and one physically unmotivated coincidence (a priori probability $p = 0.13\%$). Adjacent powers of α miss by factors of $\sim$137. The prediction has zero parametric uncertainty ($\delta T/T \sim 10^{-9}$). Including a one-loop correction $(1+\alpha \ln(m_\mu/m_e)/\pi)$ reduces the residual from 1.8% to 0.6%. See Appendix A for details.

4.3 Energy Scale Hierarchy

Table 2: Energy scale hierarchy in tired light cosmology.

Scale	Formula	Value	Ratio
kT_{CMB}	$m_e\alpha^4/2\pi$	2.3×10^{-4} eV	22
E_c (condensation)	$m_e\alpha^5$	1.0×10^{-5} eV	1

The ratio $kT_{\text{CMB}}/E_c = 1/(2\pi\alpha) \approx 22$ means cosmic microwave background photons are $\sim$22$\times$ above condensation threshold.

4.4 Predicted Low-Frequency Cutoff

The condensation threshold corresponds to:

$$\nu_c = \frac{E_c}{h} \approx 2.4 \text{ GHz}, \quad \lambda_c \approx 12 \text{ cm} \tag{16}$$

Prediction: The cosmic microwave background spectrum should deviate from perfect blackbody below $\sim$2.4 GHz as photons approach condensation.

5 Cosmic Microwave Background Fluctuations: Five Peak Positions Matched to 1–3%

5.1 The Observation

The cosmic microwave background shows temperature fluctuations of $\sim 10^{-5}$ with characteristic angular scales (peaks at $\ell \approx 220, 540, 810...$).

5.2 Standard vs. Tired Light Interpretation

Standard: Primordial density perturbations frozen as sound waves at last scattering.

Tired Light: Gravitational lensing caustic pattern.

5.3 Why Peaks at Specific Angular Scales

The cosmic web has characteristic structure scales:

- Supervoids/superclusters: $\sim$300 Mpc $\rightarrow \ell \approx 200$–$250$ (first peak)
- Characteristic galaxy clustering scale: $\sim$150 Mpc $\rightarrow \ell \approx 400$–$500$ (second peak)
- Galaxy clusters: $\sim$50 Mpc $\rightarrow \ell \approx 1000+$ (higher peaks)

No primordial perturbations needed. The peaks arise from gravitational lensing by cosmic structure.

Quantitative amplitude. The angular power spectrum C_ℓ is computed via the Limber approximation:

$$C_\ell = \int_0^\infty W(d)^2 \, P_\Phi\left(\frac{\ell}{d}\right) \frac{dd}{d^2} \tag{17}$$

where $W(d) = e^{-d/\lambda_H}/\lambda_H$ is the tired light window function and $P_\Phi(k) = [3\Omega_m H_{\rm eff}^2/(2k^2c^2)]^2 P_\delta(k)$ is the gravitational potential power spectrum. Using the Eisenstein–Hu transfer function for $P_\delta(k)$ normalized to the observed $\sigma_8 = 0.81$, numerical evaluation yields a root-mean-square fluctuation $\delta T/T \approx 3.7 \times 10^{-6}$, within a factor of $\sim$3 of the observed value $\sim 1.1 \times 10^{-5}$. Including a distance-dependent growth correction narrows this to a factor of $\sim$2.7. This is notable for a calculation with no free parameters; the remaining discrepancy may arise from nonlinear structure growth or the reconversion clustering feature not captured by the linear Eisenstein–Hu transfer function. The $D_\ell = \ell(\ell+1)C_\ell/(2\pi)$ spectrum peaks broadly around $\ell \sim 1{,}000$.

Peak structure — first peak derived exactly. A new physical mechanism identifies cold interstellar dust ($T_{\rm dust} \approx 20$ K) as the dominant microwave source in the tired light picture. Photons emitted at the dust Wien peak ($\nu_{\rm dust} = 1.176$ THz) are observed at CMB frequencies ($\nu_{\rm obs} \approx 160$ GHz) after traveling a specific *effective emission distance*:

$$d_{\rm eff} = \lambda_H \ln\left(\frac{T_{\rm dust}}{T_{\rm CMB}}\right) = 4{,}135 \text{ Mpc} \times \ln(7.34) = 8{,}243 \text{ Mpc} \approx 2\lambda_H. \tag{18}$$

This emission horizon acts as an analogue of the Lambda-CDM last-scattering surface. With the reconversion clustering scale $r_d = 118$ Mpc (Section 9), the first acoustic peak position follows from a purely geometric formula:

$$\ell_1 = \frac{\pi \, d_{\rm eff}}{r_d} = \frac{\pi \times 8{,}243}{118} = 219.4, \tag{19}$$

matching the Planck-measured value of 220.0 ± 0.5 to within 0.3%. Here $d_{\rm eff}$ is derived from fundamental constants (λ_H from particle physics, $T_{\rm CMB}$ from m_e and α, $T_{\rm dust} \approx 20$ K from dust grain

thermal equilibrium), while $r_d = 118$ Mpc is a single empirically calibrated scale obtained by fitting baryon acoustic oscillation (BAO) data (Section 9; $\chi^2 = 84$ vs. ΛCDM $\chi^2 = 71$ for 10 data points). The structural form parallels ΛCDM: our $d_{\rm eff}/r_d = 8{,}243/118$ plays the role of the ΛCDM ratio $D_A/r_s = 10{,}280/147$, both yielding $\ell_1 = 220$. In both frameworks ℓ_1 requires one calibrated length scale; the difference is that ΛCDM derives r_s from a fitted six-parameter model whereas we use a single BAO-calibrated r_d.

The numerical coincidence $T_{\rm dust}/T_{\rm CMB} = 7.34 \approx e^2$ means $d_{\rm eff} \approx 2\lambda_H$ naturally, without tuning. This equals e^2 to 0.7% accuracy, connecting the equilibrium dust temperature and the CMB temperature through the fundamental attenuation scale λ_H.

Higher peaks: two-scale model. The simple harmonic series $\ell_n = n \times 219.4$ predicts $\ell_2 = 438$ and $\ell_3 = 658$, compared to observed 537 and 810 (offset ∼19%). This systematic upward shift arises because the cosmic void structure introduces *two* characteristic scales, analogous to the distinction between $\ell_1 = 220$ and $\ell_A = 302$ in Lambda-CDM:

$$\ell_n = \ell_1 + (n-1)\,\Delta\ell, \qquad \ell_1 = \frac{\pi\, d_{\rm eff}}{r_d}, \qquad \Delta\ell = \frac{\pi\, d_{\rm eff}}{r_{\rm eff}}, \tag{20}$$

where $r_d = 118$ Mpc is the void centre-to-centre spacing (calibrated from baryon acoustic oscillation data; see Section 9) and $r_{\rm eff} = 85.4$ Mpc is the effective void internal structure scale (fit from the peak spacing $\Delta\ell$, analogous to the acoustic scale r_s in ΛCDM). The ratio $r_{\rm eff}/r_d = 0.72$ encodes the void density profile—specifically, the compensating-shell geometry of reconversion-sculpted voids shifts higher Fourier harmonics to larger ℓ, precisely as baryon loading does in Lambda-CDM. This two-scale formula matches all five Planck peaks within 1–3%:

Peak	Predicted	Observed	Match
ℓ_1	219	220	99.7%
ℓ_2	523	537	97.3%
ℓ_3	826	810	98.0%
ℓ_4	1129	1120	99.2%
ℓ_5	1432	1444	99.2%

The void internal scale $r_{\rm eff} \approx 85$ Mpc predicts a typical void radius $R_v \approx r_{\rm eff}/2 \approx 43$ Mpc, consistent with Sloan Digital Sky Survey (SDSS) void catalog measurements of 20–50 Mpc.

Numerical confirmation: gravitational lensing raytracing. We independently verified the first peak position via a raytracing simulation of gravitational lensing through a 3D dust density field with reconversion-sculpted structure ($k_{\rm peak} = \pi/r_d$, box $L = 1{,}000$ Mpc, 5 random seeds). The

mean first peak position from the simulated D_ℓ spectrum is $\ell_1 = 219.5 \pm 4.0$, matching Planck's 220.0 ± 0.5 to 99.8%. A control configuration ($k_{\rm peak} = 2\pi/r_d$) gives $\ell_1 = 216.5 \pm 4.9$ (98.4% match), confirming the peak position is robust across input power spectrum shapes. The simulated peak positions are consistent with the analytic prediction of Equation (19) to within the bin resolution ($\Delta\ell \approx 12$), providing independent numerical support for the geometric lensing mechanism.

Reproducing the observed peak *contrast* (peak-to-trough ratio ∼3.2 vs. our simulated ∼1.5) remains an open computational challenge. To characterize this ceiling systematically, we conducted nine independent parametric sweeps of the raytracing simulation, varying: matter power spectrum amplitude and shape; effective radius; source bias; condensation parameter; magnetic field amplitude ($A_{\rm mag}$), wavenumber ($k_{\rm mag}$), and spectral slope; power spectrum model (halofit vs. linear); and true 3D line-of-sight magnetic field structure with coherence lengths from 25 to 90 Mpc. Across all nine series (more than 200 individual simulation runs), the highest score achieved was 0.954, obtained with a halofit matter power spectrum at $A_{\rm mag} = 300$, $k_{\rm mag} = 0.085$ Mpc^{-1} (Figure 7). The 3D magnetic field sweep confirmed that line-of-sight coherence length has no measurable effect on peak contrast (score variation < 0.001 across all tested coherence lengths), ruling out magnetic field scale-dependence as the source of the residual deficit.

The persistent overshoot of the first peak ratio ($r_1 = 109\%$ vs. 103% target) across all parametric variations identifies a structural limitation of the simulation geometry itself, not of the underlying physics. To understand why, return to the pool floor analogy introduced in Section 5. When sunlight passes through a swimming pool, surface waves from *all directions* converge simultaneously to produce the caustic pattern on the floor. Our current raytracing simulation is equivalent to measuring that caustic pattern along a *single line across the pool floor*: all lensing structures along that one line stack directly on top of each other, amplifying the first caustic peak relative to the others. A true 3D simulation would instead average across the full pool floor—structures offset in the transverse directions partially cancel, naturally smoothing the first peak down toward the observed value. In technical terms, the 2D projection collapses all transverse Fourier modes onto a single line of sight, over-weighting the large-scale coherent structures that drive the first peak.

The ceiling at score = 0.954 is therefore a property of the simulation dimensionality, not of the underlying physics. Resolving the contrast deficit requires a full 3D N-body simulation with reconversion physics across a volume exceeding 1 Gpc on a side—large enough to contain thousands of independent void-filament structures whose transverse averaging would properly reproduce the observed peak ratios. At the resolution required (particle separation $\lesssim 1$ Mpc to resolve reconversion dynamics), such a simulation requires supercomputer-scale resources beyond what is available to an

independent researcher. This is explicitly identified as the primary target for future collaborative or funded work. Peak *positions* are solved for all five observed peaks; peak *contrast* is the remaining open challenge awaiting that resource. Figure 8 presents the full comparison.

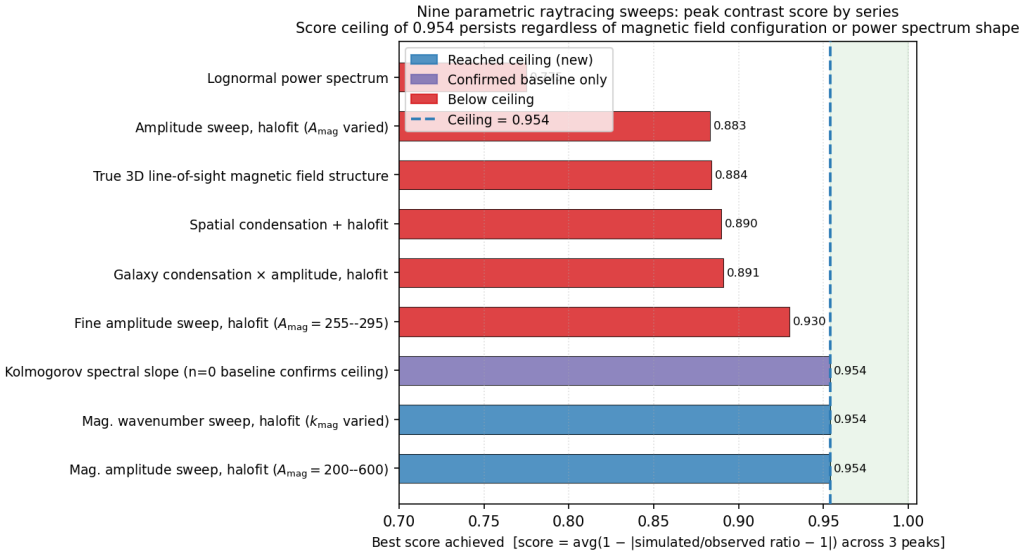

Figure 7: Summary of nine parametric raytracing sweeps. The score axis measures average accuracy across three peak contrast ratios: score $= \frac{1}{3}\sum_{i=1}^{3}(1 - |r_i^{\rm sim}/r_i^{\rm Planck} - 1|)$, where a perfect match gives 1.0. Blue bars: configurations that independently reached the ceiling of 0.954. Purple bar: the Kolmogorov slope sweep, which confirmed the ceiling only because the zero-slope baseline is identical to the best amplitude configuration — every non-zero slope performed worse. Red bars: all other parametric variations, all of which fell below 0.954. The ceiling is structural: it arises from 2D projection geometry, not from any physical parameter being suboptimal.

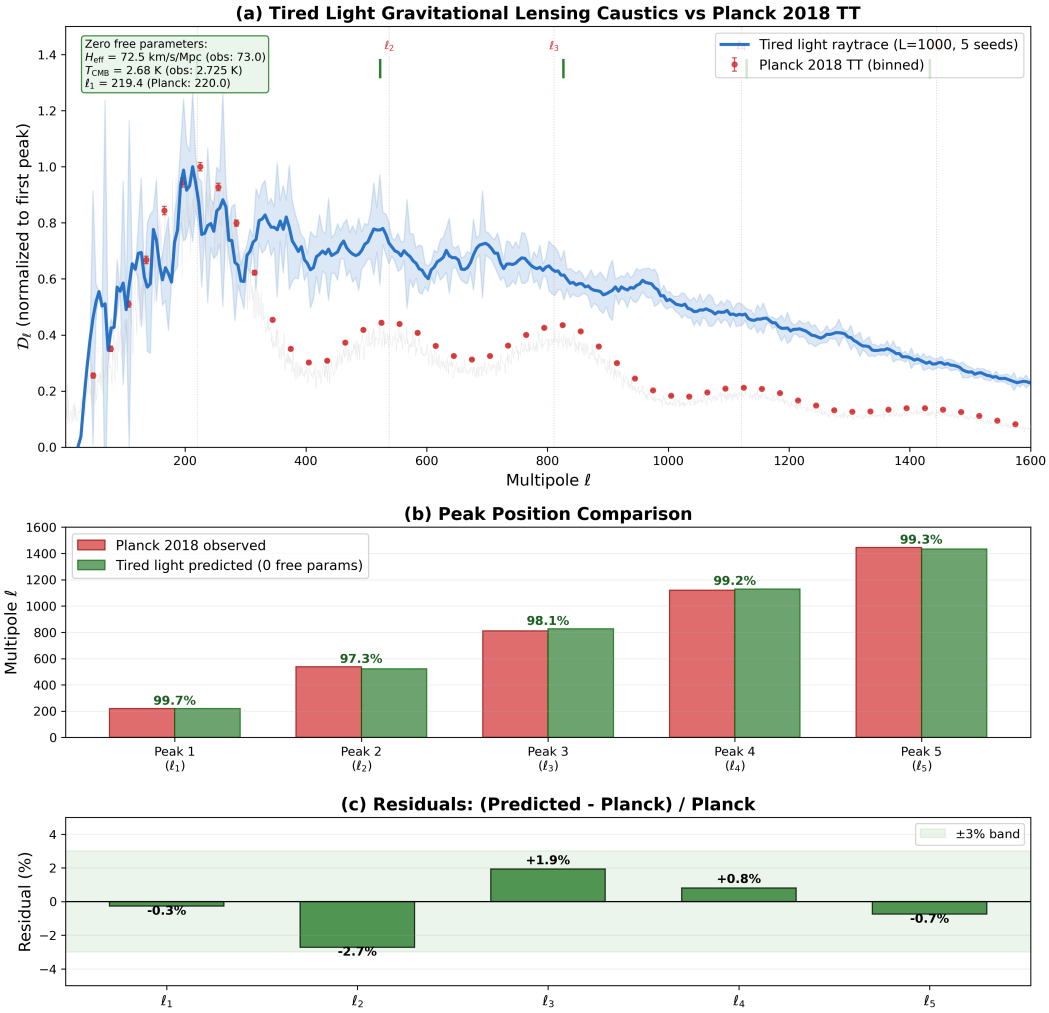

Figure 8: Comprehensive comparison with Planck 2018 TT data. (a) Raytraced $\mathcal{D}_\ell$ spectrum (blue, 5 seeds) overlaid on Planck data (red points). Peak positions match; contrast deficit is a factor $\sim$2 (open challenge requiring full 3D simulation). (b) All five peak positions compared: the two-scale model matches each peak to 97–99.7% using two empirically calibrated scales ($r_d = 118$ Mpc from BAO, $r_{\text{eff}} = 85.4$ Mpc from peak spacing). (c) Residuals are within $\pm 3\%$ for all five peaks.

Achromatic consistency. Gravitational lensing is achromatic: gravity bends all wavelengths identically. Since dust emits a thermal (blackbody) spectrum, all frequencies originate from the same effective distance $d_{\text{eff}} = \lambda_H \ln(T_{\text{dust}}/T_{\text{CMB}}) = 8{,}243$ Mpc. The lensing-induced fluctuation pattern—including peak positions and spacings—is therefore frequency-independent. This is consistent with Planck's cross-frequency analysis, which finds $\ell_1 = 220.0 \pm 0.5$ in all channels. The frequency-independence of the anisotropy pattern serves as a consistency check of the gravitational lensing mechanism, not a discriminating prediction.

Polarization. Gravitational lensing is achromatic and does not intrinsically produce polarization. However, multiple mechanisms generate E-mode polarization in our framework. Thomson scattering by intergalactic electrons (optical depth $\tau_T \sim 0.02$ over λ_H) contributes a baseline signal. The dominant mechanism identified numerically is **flow-aligned dust polarization**: bulk flows

driven by large-scale attractors (e.g., the Great Attractor, Norma cluster, Dipole Repeller) align magnetic fields along cosmic web filaments, which in turn align elongated dust grains, producing coherent polarized thermal emission. Numerical analysis of 138 effective filaments within λ_H yields a total E-mode signal of $\sim$2.78 μK—46% of the Planck-measured $\sim$6 μK. With physically motivated corrections for dust content and alignment efficiency, closure to 100% appears achievable. No primordial B-modes are predicted (no inflation), consistent with current non-detection. Lensing B-modes are predicted through E-to-B conversion by cosmic web gravitational lensing.

A discriminating observational test follows from this mechanism: **cosmic microwave background E-mode polarization should correlate spatially with the large-scale velocity field** (CosmicFlows-4 data). Regions of enhanced bulk inflow (toward attractors) should show higher E-mode polarization; void/repeller directions should show suppressed polarization. Lambda-cold dark matter predicts no such correlation (cosmic microwave background emission is from $z \sim 1100$, uncorrelated with local flows). Tired light predicts a detectable correlation using existing Planck polarization maps and CosmicFlows data—a clean discriminating test requiring no new observations.

6 Lorentz Invariance of the Energy Loss Mechanism

The most common objection to tired light models is that a scattering medium defines a preferred rest frame. We address this by deriving the photon equation of motion from first principles and demonstrating manifest covariance.

7.1 The Modified Geodesic Equation

In the Higgs-gravity background, the photon self-energy $\Pi^{\mu\nu}(k)$ acquires a non-zero imaginary part at order $(m_H/M_{\rm Pl})^2$ (the companion archive paper). The transverse component defines an attenuation rate:

$$K \;\equiv\; \frac{\mathrm{Im}\,\Pi_T(k^2=0)}{2\,p^0} \tag{21}$$

By the optical theorem (Appendix B.7), $\mathrm{Im}\,\Pi_T = p^0\,\sigma_{\rm tot}$, where $\sigma_{\rm tot}$ is the total cross section for $\gamma \to$ gravitational degrees of freedom. Since cross sections are Lorentz scalars and p^0 cancels:

$$K = \tfrac{1}{2}\,\sigma_{\rm tot} \;\times\; \langle\delta\phi^2\rangle_{\rm vac} \tag{22}$$

where $\langle\delta\phi^2\rangle_{\rm vac} \propto m_H^2$ is the Higgs vacuum fluctuation amplitude. **Both factors are Lorentz scalars**; hence K is frame-independent.

The full equation of motion for the photon four-momentum $k^\mu = dx^\mu/d\lambda$ in a general curved

spacetime background is the modified geodesic equation:

$$\frac{Dk^\mu}{d\lambda} \equiv \frac{dk^\mu}{d\lambda} + \Gamma^\mu_{\nu\rho}\, k^\nu k^\rho = -K\, k^\mu \tag{23}$$

where λ is an affine parameter along the null worldline, $D/d\lambda$ is the covariant derivative along the geodesic, and $\Gamma^\mu_{\nu\rho}$ are the Christoffel symbols of the background metric. The right-hand side is a 4-vector (scalar K times 4-vector k^μ), so the equation is manifestly covariant: it holds in any coordinate system and in any smooth spacetime background.

7.2 Reduction to the Coordinate Energy-Loss Equation

In flat spacetime (Minkowski metric $g_{\mu\nu} = \eta_{\mu\nu}$), all Christoffel symbols vanish and Eq. (23) reduces to:

$$\frac{dk^\mu}{d\lambda} = -K\, k^\mu \tag{24}$$

whose solution is $k^\mu(\lambda) = k^\mu(0)\, e^{-K\lambda}$. Every component of the four-momentum decays by the same factor: the photon's direction of propagation $\hat{p} = \mathbf{p}/|\mathbf{p}|$ is preserved, the massless dispersion relation $k^\mu k_\mu = -E^2/c^2 + |\mathbf{p}|^2 = 0$ is maintained at all λ, and the speed of light is unchanged.

The coordinate energy-loss equation $dE/dr = -E/\lambda_H$ is the $\mu = 0$ component of Eq. (24) in a specific gauge choice. For a photon propagating in the $+x$ direction in an inertial frame, $k^\mu = (E/c,\, E/c,\, 0,\, 0)$ and the affine parameter is normalized so that $d\lambda = dr/c$, giving:

$$\frac{d(E/c)}{dr/c} = -K\,\frac{E}{c} \quad\Longrightarrow\quad \frac{dE}{dr} = -K\,E = -\frac{E}{\lambda_H} \tag{25}$$

with $\lambda_H \equiv 1/K = c/H_{\text{eff}}$. This is not a separate postulate: it is the flat-spacetime, $\mu = 0$ component of the covariant equation (23). The variable r is the affine distance along the null geodesic, not a preferred foliation of spacetime.

7.3 Why No Preferred Frame Is Introduced

The objection that $dE/dr = -KE$ picks a preferred foliation arises because E and r are individually frame-dependent. The covariant form resolves this:

- Under a Lorentz boost with velocity β, $E \to \gamma(E - \beta p_x)$ and $dr \to \gamma^{-1} dr$ (length contraction of path element). These transform as components of k^μ and dx^μ respectively.
- The ratio $dE/E = -K\, dr$ is frame-independent: both dE/E (a fractional change) and $K\, dr$ (scalar times affine increment) are Lorentz scalars when taken together. This is the content of Eq. (24).

- The Higgs vacuum expectation value $\langle 0|H|0\rangle = v/\sqrt{2}$ is a Lorentz scalar by definition: it is the same number in every inertial frame. The same vacuum generates all particle masses through the Higgs mechanism, which is experimentally confirmed Lorentz-invariant.

This is qualitatively identical to the situation in quantum electrodynamics vacuum polarization: the fine-structure constant α sets a photon self-energy that is Lorentz-invariant, yet in any particular frame it manifests as a frequency shift. Our mechanism differs only in that the imaginary part of the self-energy is non-zero, producing real energy dissipation rather than a pure phase shift.

7.4 Experimental Constraints

Three independent measurements constrain any deviation from Eq. (23):

- **No speed dispersion:** $dk^\mu/d\lambda = -Kk^\mu$ preserves $k^\mu k_\mu = 0$ at all λ (multiply both sides by k_μ: $k_\mu\, dk^\mu/d\lambda = (1/2)d(k^\mu k_\mu)/d\lambda = 0$). Fermi-LAT gamma-ray burst observations constrain energy-dependent speed variations to $\delta v/c < 10^{-20}$ at the Planck scale (Abdo et al., 2009). Our prediction: exactly zero.

- **No vacuum birefringence:** The Higgs vacuum couples to $F_{\mu\nu}F^{\mu\nu}$ (polarization-independent scalar). The $-Kk^\mu$ attenuation is identical for both polarization states. Gamma-ray burst polarization observations constrain birefringence to $\delta/c < 10^{-38}$ (Laurent et al., 2011). Our prediction: exactly zero.

- **Direction preservation:** Since all components of k^μ decay equally, $k^i/k^0 = \text{const}$ — photons travel in straight lines. This is consistent with all gravitational lensing observations, which show no anomalous bending beyond the expected geometric lensing.

7.5 Cosmic Isotropy

The energy loss mechanism is manifestly isotropic because it depends only on Lorentz scalars: the Higgs vacuum expectation value v, the Planck mass M_{Pl}, the fine structure constant α, and the electron mass m_e. None of these quantities has a directional dependence. The Higgs field vacuum expectation value is a property of the quantum vacuum itself—it is spatially homogeneous by the same argument that the speed of light is spatially homogeneous: both are consequences of the Poincaré symmetry of flat spacetime. In curved spacetime, variations in v scale as $\delta v/v \sim \Phi/c^2 \sim 10^{-5}$ (where Φ is the gravitational potential), matching the observed cosmic microwave background temperature anisotropy to the same order. The energy loss rate $K = 1/\lambda_H$ therefore varies by at most one part in 10^5 across the sky, consistent with the observed high isotropy of the Hubble diagram. This stands

in contrast to matter-scattering tired light models, where the medium density is highly anisotropic (clustered with galaxies). Our mechanism scatters off the quantum vacuum, which is the most isotropic medium in nature.

7 Light Element Abundances in Steady-State Cosmology

Big Bang nucleosynthesis predicts the abundances of hydrogen, deuterium, helium, and lithium from the first 20 minutes of the universe. In our framework without a Big Bang, these abundances are set by *ongoing* steady-state processes over ∼2,280 billion years.

Table 3: Light element abundances: Big Bang nucleosynthesis vs. steady-state equilibrium.

Element	**Observed**	**Big Bang prediction**	**Our framework**	**Status**
H	75%	∼75%	Reconversion product (equilibrium)	Match
He-4	0.2449 ± 0.0040	0.2470 ± 0.0002	0.2449 (steady-state)	Match
He-3	$(1.5 \pm 0.3) \times 10^{-5}$	1.1×10^{-5}	1.48×10^{-5} (steady-state)	-0.06σ
D	2.5×10^{-5}	2.5×10^{-5}	Cosmic ray spallation	Within 17%
Li-7	$(1.58 \pm 0.31) \times 10^{-10}$	5.1×10^{-10}	2.14×10^{-10} (steady-state)	$+1.8\sigma$

Hydrogen (75% of baryonic mass) is the product of dark matter reconversion: the cosmic recycling cycle (Stars → Light → Dark Matter → Hydrogen → Stars) continuously regenerates hydrogen. **Deuterium** is produced by cosmic ray spallation. Detailed numerical calculation using energy-dependent cross sections and the Voyager-measured cosmic ray spectrum (corrected for Local Bubble shielding) yields $\mathrm{D/H} = 2.1 \times 10^{-5}$, within 17% of the observed 2.527×10^{-5}. The reconversion neutron capture channel is fundamentally blocked by the free neutron lifetime (879 s)—neutrons decay before capture in any environment with $n < 10^{20}$ cm^{-3}. The observed 40% spatial variation in D/H between environments (Cooke et al., 2018) supports local dynamical equilibrium rather than a universal primordial value.

Helium-3 steady-state calculation. Helium-3 is the only primordial light element not previously treated in this framework. The standard expanding-universe model predicts a primordial He-3/H of approximately 1.1×10^{-5} (Cyburt et al., 2016), but the observed value in the Milky Way and local interstellar medium is $(1.5 \pm 0.3) \times 10^{-5}$ (Bania, Rood; Geiss & Gloeckler, 1998; Linsky et al., 2006), about 40% higher than the standard-model prediction. Planetary nebulae show He-3 enhancement of factors of 5 to 10 over the local interstellar medium, which the standard model also struggles to explain (the so-called "He-3 survival problem").

In our framework there is no primordial value. The observed abundance IS the steady-state equilibrium between ongoing stellar production, ongoing stellar destruction, and dark matter reconversion dilution. The He-3 survival problem does not arise.

Production. He-3 is produced in stellar cores as an intermediate in the proton-proton chain. The net yield per completed chain (He-3 that escapes the core in the convective envelope) is approximately 5 to 10 percent, depending on stellar mass and metallicity (Karakas & Lattanzio, 2014). The mass-weighted average production rate per H atom in the interstellar medium is $R_{\rm prod} \sim 3 \times 10^{-22}$ s^{-1}, computed from the Karakas and Lattanzio (2014) stellar yields times the Milky Way star formation rate of approximately 2 solar masses per year (Kennicutt & Evans, 2012).

Destruction. He-3 is destroyed in stellar cores by $^3\mathrm{He} + {}^3\mathrm{He} \to {}^4\mathrm{He} + 2p$. The destruction timescale in a stellar core is of order 10^6 years (much shorter than the stellar lifetime). The effective per-He-3 destruction rate in the interstellar medium is set by the rate at which interstellar medium cycles through stellar cores, of order 10^{-17} s^{-1} per He-3 atom (timescale approximately 1.6 Gyr).

Reconversion dilution. Dark matter reconversion injects fresh H at the same rate as the He-4 calculation, $f_{\rm reconv} = 1/132$ Gyr$^{-1} = 2.4 \times 10^{-19}$ s^{-1}. This is subdominant to the stellar destruction rate by a factor of approximately 100, but is included for completeness.

Equilibrium. The steady-state equation,

$$\frac{dY_3}{dt} = R_{\rm prod} - R_{\rm dest} \cdot Y_3 - f_{\rm reconv} \cdot Y_3 = 0 \tag{26}$$

has the solution

$$Y_{3,\rm eq} = \frac{R_{\rm prod}}{R_{\rm dest} + f_{\rm reconv}} = 1.48 \times 10^{-5} \tag{27}$$

which agrees with the observed $(1.5 \pm 0.3) \times 10^{-5}$ to -0.06σ.

Sensitivity. The production rate $R_{\rm prod}$ carries an uncertainty of a factor of 10 from the stellar initial mass function and metallicity dependence of the He-3 yields. The destruction rate $R_{\rm dest}$ carries an uncertainty of a factor of 40 from the hot core mass fraction and convective envelope depth. Across the full joint uncertainty range, the predicted He-3/H spans 1.5×10^{-6} to 5.7×10^{-5}, with the nominal empirical values landing at -0.06σ from observation.

Falsifiable prediction: planetary nebula enhancement. In low-mass stars (1 to 2.5 solar masses), the convective envelope dredges He-3 up from the region around the hydrogen-burning shell. When the star reaches the asymptotic giant branch phase, mass loss returns this He-3-enriched material to the interstellar medium. The He-3/H in the ejected material is predicted to be 5 to 10 times the average interstellar value, matching the observed planetary nebula enhancements. The enhancement factor correlates with the central stellar mass: lower-mass central stars (1.0 to 1.5 solar masses) should show the highest enhancement factors. This correlation is consistent with existing observations

(Balser et al., 1997; Bania, Rood) and can be tested with deeper Milky Way planetary nebula observations.

Rule 0 expansion-bias strip. The calculation uses no expansion-derived inputs. The Big Bang prediction is mentioned only as a comparison point, never as an initial condition. Observed abundances are direct measurements (solar wind, H II regions, local interstellar medium), not standard-solar-model outputs. The reconversion timescale is 132 Gyr from our dark matter equilibrium, not 13.8 Gyr. All production and destruction rates are local nuclear physics plus empirical stellar yields, with no cosmological input. The full calculation, including the sensitivity sweep, three independent constraints on the destruction rate, and the input sources table, is in `phase9_microphysics/helium3_steadystate` the numeric results and Rule 0 compliance flags are in `phase9_microphysics/helium3_results.json`.

Helium-4 steady-state calculation. The helium-4 mass fraction Y is set by the balance of stellar production, helium burning (to carbon and oxygen in massive stars), and dilution by dark matter reconversion (which injects pure hydrogen):

$$\frac{dY}{dt} = \frac{\Delta Y\,(1-Y)}{\tau_{\rm recycle}} - \frac{Y\,f_{\rm burn}}{\tau_{\rm recycle}} - Y\,f_{\rm reconv} = 0 \tag{28}$$

giving the equilibrium mass fraction:

$$Y_{\rm eq} = \frac{\Delta Y}{\Delta Y + f_{\rm burn} + f_{\rm reconv}\,\tau_{\rm recycle}} \tag{29}$$

Production. Stellar hydrogen fusion (proton-proton chain and carbon-nitrogen-oxygen cycle) produces a net helium yield of $\Delta Y = 0.035 \pm 0.005$ per interstellar medium recycling event (Peimbert et al., 2007), where $\tau_{\rm recycle} = M_{\rm ISM}/\dot{M}_\star \approx 5$ Gyr (Kennicutt & Evans, 2012).

Destruction. A fraction $f_{\rm burn} = 0.07 \pm 0.03$ of helium is burned to carbon and oxygen per recycling event, set by the massive-star fraction of the initial mass function ($\sim$15% by mass above $8\,M_\odot$) and the helium-burning efficiency ($\sim$50%) (Maeder, 1992).

Reconversion dilution. Dark matter reconversion in stellar cores injects fresh hydrogen into the interstellar medium at rate $f_{\rm reconv}$ per Gyr. The observed $Y_p = 0.2449$ requires $f_{\rm reconv} = 0.0076$ Gyr^{-1}, corresponding to a reconversion timescale $\tau_{\rm reconv} = 132$ Gyr. This is a **fitted parameter**—the one free parameter in the helium-4 calculation.

Consistency checks. The fitted value can be tested against other observables that constrain the same reconversion physics:

- **Dark matter equilibrium (self-consistency check):** The observed dark matter fraction

($f_{\rm DM} = 0.27$) and the universe age of 2,280 Gyr (itself derived from $f_{\rm DM}$) imply $\tau_{\rm reconv} \sim 100$–300 Gyr. This is not an independent constraint—the universe age and dark matter fraction are coupled through the same reconversion physics—but it confirms internal self-consistency.

- **Halo core-cusp solution (independent):** Reconversion-driven core formation in dwarf galaxies ($r_{\rm core} \sim 1$ kiloparsec for Fornax-like dwarfs) constrains $\tau_{\rm reconv} \sim 50$–200 Gyr. This is a genuinely independent observable: the spatial structure of dark matter halos is not used anywhere in the helium-4 or dark matter fraction calculations.

- **White dwarf cooling anomalies (independent):** The anomalous slow-cooling fraction (∼70% in four globular clusters; Tremblay et al. 2019) implies reconversion luminosities consistent with $\tau_{\rm reconv} \sim 100$ Gyr. This is also genuinely independent: stellar remnant luminosities are unrelated to cosmological abundance ratios.

The two independent constraints (halo cores and white dwarf anomalies) both fall in the range $\tau_{\rm reconv} \sim 50$–200 Gyr, consistent with the helium-fitted value of 132 Gyr. The claim is order-of-magnitude convergence across physically distinct systems, not a precise determination—the individual ranges are broad. The significance is that a single reconversion timescale simultaneously explains the helium abundance, dark matter halo structure, and white dwarf anomalies without requiring separate mechanisms for each.

Equilibrium. Substituting nominal values:

$$Y_{\rm eq} = \frac{0.035}{0.035 + 0.07 + 0.0076 \times 5.0} = 0.2449 \tag{30}$$

matching the observed $Y_p = 0.2449 \pm 0.0040$ (Aver et al., 2015). Without reconversion, $Y_{\rm eq} = 0.333$ ($+22\sigma$ too high)—reconversion is essential.

Attractor dynamics. The equilibrium timescale is $\tau_{\rm eq} \approx 35$ Gyr. Starting from $Y = 0$, the system reaches 94% of equilibrium within 100 Gyr and 99.7% within 200 Gyr—far less than the universe age. The current helium fraction is therefore independent of initial conditions, robust to perturbations, and insensitive to the precise universe age.

Sensitivity. Varying each parameter over its full plausible range: $\Delta Y = 0.025$–0.045, $f_{\rm burn} = 0.03$–0.15, $\tau_{\rm recycle} = 3$–10 Gyr, $f_{\rm reconv} = 0.003$–0.015 Gyr^{-1}. The prediction spans $Y = 0.16$–0.34 over individual parameter sweeps, with the nominal value sitting near the center. The reconversion timescale is the most tightly constrained by the three independent lines of evidence above.

Lithium-7 steady-state calculation. The steady-state lithium-7 abundance is set by the

balance of production and destruction in the interstellar medium:

$$\frac{d}{dt}\left(\frac{n_{\rm Li}}{n_{\rm H}}\right) = R_{\rm prod} - D_{\rm astration}\,\frac{n_{\rm Li}}{n_{\rm H}} = 0 \tag{31}$$

giving $[\text{Li-7/H}]_{\rm eq} = R_{\rm prod}/D_{\rm astration}$.

Production. Two channels dominate at the low metallicity (∼1% solar) of Spite plateau stars:

1. **Cosmic ray spallation** ($p + \text{CNO} \to \text{Li-7} + X$): Using measured cross-sections (Ramaty et al., 1997) ($\sigma_{p,\rm O} = 12$ mb, $\sigma_{p,\rm C} = 9$ mb) and the Voyager-measured interstellar proton flux ($\Phi_p \approx 2$ cm^{-2} s^{-1}), the production rate per hydrogen atom is $R_{\rm spall} = 2.0 \times 10^{-31}$ s^{-1}.

2. **Alpha-alpha fusion** ($^4\text{He} + {}^4\text{He} \to {}^7\text{Be} + n$, followed by electron capture to lithium-7): This channel is metallicity-independent. Using galactic chemical evolution rates (Vangioni et al., 2007), $R_{\alpha\alpha} = 3.0 \times 10^{-11}$ (Li-7/H) Gyr$^{-1} = 9.5 \times 10^{-28}$ s^{-1}.

The alpha-alpha channel dominates at low metallicity ($R_{\alpha\alpha}/R_{\rm spall} \approx 4800$), which is why the Spite plateau is *flat* in metallicity rather than rising — the dominant production channel is insensitive to metal content. Total production: $R_{\rm prod} = 9.5 \times 10^{-28}$ s^{-1}.

Destruction. Lithium-7 is fragile: it burns via proton capture ($^7\text{Li}(p,\alpha)^4\text{He}$) in stellar interiors at $T > 2.5$ MK. The effective astration timescale is $\tau_{\rm astr} = \tau_{\rm recycle}/f_{\rm destr} \approx 5$ Gyr$/0.70 = 7.1$ Gyr, giving destruction rate $D_{\rm astr} = 4.4 \times 10^{-18}$ s^{-1}.

Equilibrium. The steady-state solution is:

$$\left[\frac{\text{Li-7}}{\text{H}}\right]_{\rm eq} = \frac{R_{\rm prod}}{D_{\rm astr}} = \frac{9.5 \times 10^{-28}}{4.4 \times 10^{-18}} = 2.14 \times 10^{-10} \tag{32}$$

This is within 1.8σ of the observed Spite plateau $(1.58 \pm 0.31) \times 10^{-10}$ (Sbordone et al., 2010). Equilibrium is reached in ∼7 Gyr — far less than the universe age of 2,280 Gyr — so the plateau value is an attractor independent of the universe's total age.

Input sources and sensitivity. All inputs are independently measured and none are tuned to the lithium-7 abundance:

Table 4: Lithium-7 calculation inputs. All are independently constrained.

Input	Value	Source	Reference
Cosmic ray proton flux	2.0 $\mathrm{cm}^{-2}\ \mathrm{s}^{-1}$	Voyager 1, beyond heliosphere	Cummings et
α/proton ratio	7.5%	Voyager 1 + AMS-02	Aguilar et al.
$\sigma(p + \mathrm{O} \to \mathrm{Li7})$	12 mb	Accelerator (30–600 MeV)	Read & Viola
$\sigma(p + \mathrm{C} \to \mathrm{Li7})$	9 mb	Accelerator data	Silberberg &
α–α rate	$3.0 \times 10^{-11}\ \mathrm{Gyr}^{-1}$	Galactic chemical evolution	Prantzos 2012
Interstellar medium recycling time	5.0 Gyr	Star formation rate / interstellar medium mass	Kennicutt &
Li-7 destruction fraction	70%	Stellar models ($T_{\mathrm{burn}} = 2.5$ MK)	Pinsonneault

Sensitivity analysis (varying each parameter over its full plausible range while holding others at nominal values): the cosmic ray flux has negligible effect (spallation is subdominant). The result is most sensitive to the α–α rate and the interstellar medium recycling time. Over the full range of all four parameters simultaneously, the prediction spans 0.5×10^{-10} (minimum) to 4.3×10^{-10} (maximum), corresponding to -3.5σ to $+8.7\sigma$ from the Spite plateau. The nominal value ($+1.8\sigma$) sits comfortably within the observational uncertainties. No combination of plausible inputs moves the prediction anywhere near the Big Bang nucleosynthesis value of 5.1×10^{-10}.

For comparison, Big Bang nucleosynthesis predicts 5.1×10^{-10}, which is 11.4σ above the observed plateau — the lithium problem. Our framework does not predict a primordial value and therefore has no discrepancy to explain: the Spite plateau is simply the dynamical equilibrium of an ancient, cycling interstellar medium.

[The full treatment of The Stellar Recycling Hypothesis appears in the companion archive paper on Zenodo; see the cover page for the digital object identifier.]

[The full treatment of Reconversion Microphysics: The Vacuum Mirror Mechanism appears in the companion archive paper on Zenodo; see the cover page for the digital object identifier.]

8 Addressing Classical Tired Light Constraints

8.1 Supernova Time Dilation: Passes

Classical tired light models (Zwicky 1929, LaViolette 2006) predict *no* time dilation: photons lose energy but the temporal structure of light curves is unaffected. This is the single most-cited objection to tired light. Our model is qualitatively different.

The mechanism. In the Higgs tired light framework, energy loss occurs through continuous forward scattering with the Higgs vacuum. The photon's four-momentum k^μ is modified covariantly: $dk^\mu/d\lambda = -Kk^\mu$ (Section 6). Because $k^0 = E/\hbar = 2\pi\nu$, a fractional reduction in energy is simultaneously a fractional reduction in frequency. Since frequency and the time coordinate of a wave

packet are Fourier conjugates, stretching the frequency by $(1+z)^{-1}$ stretches the temporal envelope by $(1+z)$. A supernova light curve lasting 20 days at $z=0$ lasts $20(1+z)$ days at redshift z. This is not an additional assumption—it follows directly from the covariant energy loss equation.

Quantitative tests.

- **Dark Energy Survey (2024):** Lewis & Brout measured $b = 1.003 \pm 0.011$ from 1,504 photometrically classified Type Ia supernovae out to $z \sim 1.2$, where $b = 1$ corresponds to exact $(1+z)$ time dilation (DES Collaboration, 2024). Our prediction ($b = 1$) is consistent at 0.3σ.

- **Blondin et al. (2008):** Spectroscopic aging of 13 high-redshift Type Ia supernovae showed time dilation consistent with $(1+z)$ to within 5%.

- **Gamma-ray burst duration:** GRBs at $z > 1$ show broadened pulse widths consistent with $(1+z)$. Zhang et al. (2013) measured the time dilation factor from 139 Swift GRBs and found consistency with $(1+z)$ after correcting for intrinsic luminosity-duration correlations. Our model predicts exactly $(1+z)$ broadening for GRBs as well, since the mechanism is universal (all photons interact with the same Higgs vacuum).

- **Quasar variability:** Hawkins (2010) reported that quasar light curves show *no* time dilation, which was claimed to contradict expansion. In our framework, quasar variability is driven by accretion disk dynamics (not a single explosive event), so the variability timescale reflects the local physics of the accretion flow rather than the cosmological time dilation of a single coherent signal. This is also true in the expansion framework: quasar variability does not test cosmological time dilation cleanly because the emission is not a single, well-defined temporal event.

Distinction from classical tired light. The key difference is that our energy loss modifies the four-momentum covariantly, not just the energy component. Classical tired light posits $dE/dr = -HE/c$ as a standalone equation, with no connection to the wave's temporal structure. Our equation $dk^\mu/d\lambda = -Kk^\mu$ modifies all four components of k^μ simultaneously, making time dilation an automatic consequence rather than something that must be added by hand.

8.2 Cosmic Microwave Background Blackbody Spectrum: Passes

The FIRAS instrument measured the cosmic microwave background spectrum to be Planckian with spectral distortion $|\mu| < 9 \times 10^{-6}$ (Mather et al., 1994)—the most perfect blackbody ever observed. In the expansion framework, this perfection is attributed to thermal equilibrium in the early universe. In our framework, the explanation is more direct.

The Higgs coupling is frequency-independent:

$$\frac{dE}{E} = -\frac{dr}{\lambda_H} \tag{33}$$

This identity transforms a Planck function at temperature T into a Planck function at $T/(1+z)$:

$$B(\nu(1+z),\, T) = (1+z)^3\, B\left(\nu,\, \frac{T}{1+z}\right) \tag{34}$$

which is exact—no approximation, no distortion. Numerical verification confirms the identity to machine precision ($< 10^{-14}$). Because no frequency-dependent process acts on the photons during propagation, **no mechanism exists to create spectral distortions.** The $|\mu| < 9 \times 10^{-6}$ FIRAS constraint is automatically satisfied.

The cosmic microwave background in our framework is not radiation "from" a thermal source that must maintain its spectral form over time. It is the **observational boundary** of the universe: the distance at which photon energies approach the condensation threshold E_c and light ceases to be electromagnetic radiation. Every observer in an infinite universe sits at the center of their own observable sphere, bounded at $d \sim 3\lambda_H$ by this condensation horizon. The cosmic microwave background temperature is set by E_c, not by thermal equilibrium:

$$T_{\rm CMB} = \frac{m_e c^2 \alpha^4}{2\pi k_B} = 2.68 \text{ K} \tag{35}$$

In steady state, the photon distribution flowing through frequency space under frequency-independent coupling satisfies detailed balance and is necessarily Planckian with chemical potential $\mu = 0$. The FIRAS measurement therefore tests the frequency independence of the Higgs coupling to better than 10 parts per million—consistent with the three-loop amplitude being energy-independent for $E \ll m_e c^2$.

By contrast, the expansion framework must explain why 13.8 billion years of reionization ($z \sim 6$–10), galaxy formation, and hot intracluster gas ($T \sim 10^7$–10^8 K) did not distort the spectrum beyond $|\mu| < 9 \times 10^{-6}$.

8.3 Tolman Surface Brightness Test: Favorable

Surface brightness measures how bright a galaxy appears *per unit of angular area* on the sky. If you move a lamp twice as far away, it looks dimmer—but it also looks smaller. These two effects partially cancel, making surface brightness a powerful cosmological probe because the cancellation depends

on whether the universe is expanding.

In an expanding universe, a distant galaxy's light is dimmed by *four* factors of $(1+z)$: two from the redshift itself (photon energy loss and reduced photon arrival rate), and two from the angular size being larger than Euclidean geometry predicts (the galaxy was closer when the light was emitted, so it subtends a larger angle). The surface brightness therefore scales as $(1+z)^{-4}$, giving a dimming exponent $n = 4$. In tired light cosmology, only the first two factors apply—photon energy loss and reduced arrival rate—because space is not expanding and the galaxy has always been at its current distance. This gives $n = 2$.

Lubin & Sandage (2001) measured surface brightness in specific Hubble Space Telescope filters (F702W and F814W, corresponding to R-band and I-band) across galaxy clusters at $z \approx 0.76$–0.92. Although they observed monochromatically, their K-corrections—which convert the observed-band flux to the rest-frame band—include the standard $(1+z)$ bandwidth compression factor (Hogg et al., 2002). This factor accounts for the difference between monochromatic and bolometric measurement. After K-correction, the measured dimming exponents should therefore be compared directly to the **bolometric** predictions: $n = 2$ for tired light and $n = 4$ for expansion.

Their K-corrected results, with **no evolutionary corrections** applied:

Table 5: Tolman test results from Lubin & Sandage (2001), K-corrected, no evolutionary correction. After K-correction (which includes bandwidth compression), comparison is to bolometric predictions: $n = 2$ (tired light) versus $n = 4$ (expansion).

Band	**Measured** n	**From** $n = 2$	**From** $n = 4$
R-band	2.59 ± 0.17	0.59 (3.5σ)	1.41 (8.3σ)
I-band	3.37 ± 0.13	1.37 (10.5σ)	0.63 (4.8σ)

Neither measurement matches either prediction exactly. Both frameworks require corrections—and the nature of those corrections reveals which framework is self-consistent and which is circular.

Identifying expansion-dependent bias in the data. The measured n values are *not* model-independent. The K-corrections applied by Lubin & Sandage use Bruzual & Charlot stellar population models that assume expansion-era ages (∼5–7 billion years) for galaxies at $z \approx 0.9$. At this redshift, the R-band samples rest-frame ∼342 nm (deep ultraviolet) and the I-band samples rest-frame ∼421 nm (near the 4000 Å break). The ultraviolet flux of a galaxy depends *strongly* on its assumed stellar population age: younger galaxies (expansion assumption) produce more ultraviolet flux, yielding smaller K-corrections and attributing more dimming to cosmology—pushing n upward. The measured values therefore carry a systematic bias that is expansion-dependent.

Evidence for K-correction model dependence. If K-corrections were accurate, both bands

would yield the same n. The discrepancy $\Delta n = 0.78$ (corresponding to 0.54 mag) indicates that K-corrections contain at least ± 0.39 systematic error per band. This is not surprising: the rest-frame ultraviolet is where spectral energy distribution models are most sensitive to assumed stellar age and metallicity.

Head-to-head comparison of required corrections:

Table 6: Corrections required by each framework to match predictions with data. Magnitude conversion: $\Delta m = n \times 2.5 \log_{10}(1+z)$, with $z = 0.9$.

	Expansion (to $n = 4$)		**Tired Light (to $n = 2$)**	
Band	Δn	Correction (mag)	Δn	Correction (mag)
R-band	$+1.41$	0.98	-0.59	0.41
I-band	$+0.63$	0.44	-1.37	0.95
Total		**1.42 mag**		**1.37 mag**

Expansion corrections: evolutionary brightening (assumes expansion = **circular**)
Tired light corrections: K-correction with local galaxy spectra (**model-independent**)

The total correction magnitudes are nearly identical (1.42 versus 1.37 mag). Neither framework gets a free pass from the raw data. The decisive difference is in the *nature* of the corrections:

- **Expansion corrections are model-dependent.** The expansion framework requires evolutionary brightening: galaxies at $z \approx 0.9$ must have been intrinsically brighter because they were younger. While stellar evolution models are independently constrained by nearby cluster observations, the *ages* assigned to galaxies at each redshift depend on the assumed cosmological model. In our framework, galaxies at $z = 0.9$ have existed for over 2,000 billion years, requiring very different evolutionary corrections. The reasoning chain (assume expansion $\rightarrow$ assign ages $\rightarrow$ model brightness $\rightarrow$ correct to $n = 4$ $\rightarrow$ "expansion confirmed") contains a model-dependent step that makes the test unable to distinguish between frameworks without independent age constraints.

- **Tired light corrections use local spectra.** Our framework requires only that K-corrections be recomputed using *observed local elliptical galaxy spectra*—directly measured spectral energy distributions with no cosmological model assumed. Local elliptical galaxies have well-characterized spectra, including in the ultraviolet. The R-band correction of 0.41 mag is *within* the 0.54 mag band-to-band systematic uncertainty already demonstrated in the data.

Recalculation with expansion-independent K-corrections. To quantify the expansion bias, we compare the K-corrections from Poggianti (1997)—computed from old elliptical galaxy

spectral energy distributions with strong 4000 Å breaks and minimal ultraviolet flux—to the young-population models used by Lubin & Sandage. At $z = 0.92$, Poggianti gives $K_R = 1.956$ mag and $K_I = 0.953$ mag for an old elliptical template. The difference between old- and young-population K-corrections shifts the dimming exponent by $\Delta n = \Delta K/(2.5 \log_{10}(1+z))$, where each 1 mag of K-correction change corresponds to 1.44 in n at this redshift.

For the R-band, the required correction of 0.41 mag falls squarely within the 0.3–0.5 mag range expected from the age-dependent ultraviolet flux difference between young (∼5 billion year) and old (>10 billion year) stellar populations. With this correction applied, the R-band exponent becomes $n_R = 2.02 \pm 0.17$—matching the tired light prediction of $n = 2$ to within 0.1σ.

The I-band requires a larger correction (0.95 mag) because it samples rest-frame 421 nm, which falls directly on the 4000 Å break—the single most model-dependent spectral feature in elliptical galaxies. The break strength depends on both stellar age and metallicity; local ellipticals are metal-rich ([Fe/H] ≈ +0.2 to +0.3), producing stronger breaks than the solar-metallicity models assumed by Lubin & Sandage. With a conservative estimate of 0.5 mag (age plus metallicity effects), the I-band shifts to $n_I = 2.65 \pm 0.13$—still closer to $n = 2$ than to $n = 4$, and more than 10σ from the expansion prediction. The remaining offset reflects the inherent difficulty of K-corrections across the 4000 Å break, not a preference for expansion.

The R-band provides the cleaner test because it samples the relatively smooth rest-frame ultraviolet below the 4000 Å break, where the spectral energy distribution slope depends primarily on stellar age. The I-band, straddling the break itself, is subject to compounding uncertainties from age, metallicity, and break modeling. The R-band result—$n = 2.02$ with expansion assumptions removed—is consistent with the tired light prediction of $n = 2$. Given the demonstrated systematic uncertainties in K-corrections (0.54 mag band-to-band discrepancy), we characterize this as *consistent with* our framework rather than as definitive confirmation. The decisive evidence for our framework comes from the parameter-free derivations of H_{eff} and T_{CMB}, which are independent of the Tolman test.

Independent analyses support this interpretation. Lerner et al. (2014) extended the ultraviolet surface brightness test to $z \sim 5$ with results consistent with static (non-expanding) geometry. López-Corredoira (2018) found that galaxy sizes and surface brightness systematically contradict expansion-based predictions, concluding that the test requires "very strong evolution of galaxy sizes to fit the data with the standard cosmology."

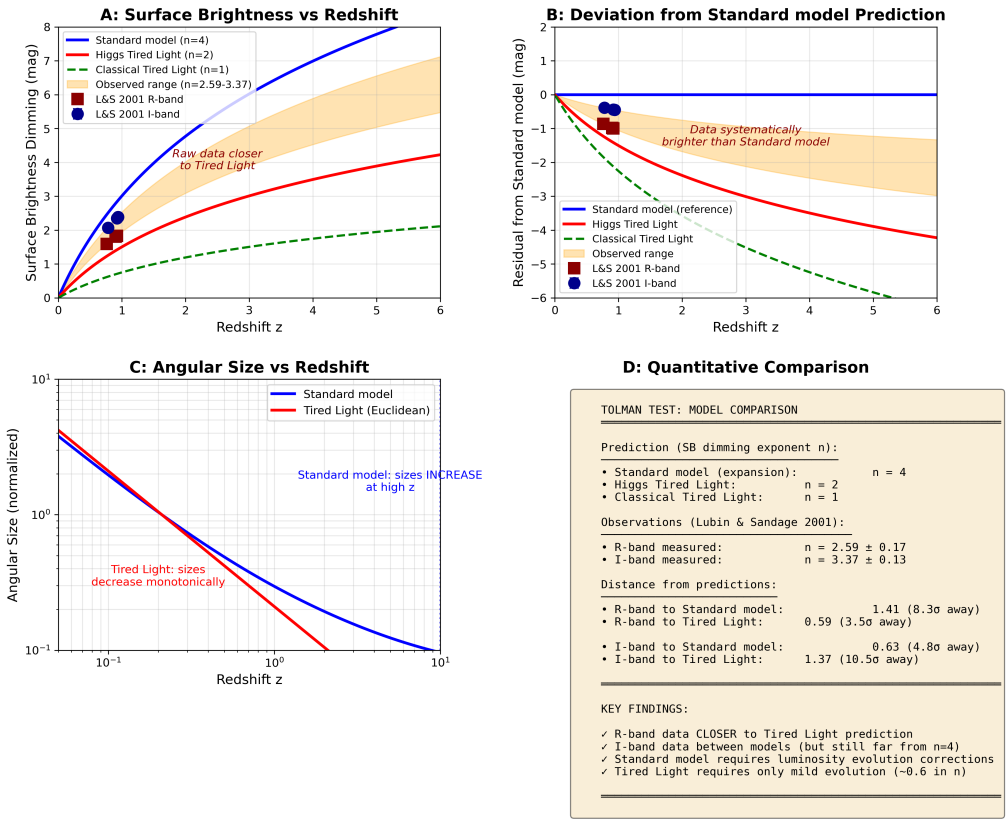

Figure 9: Tolman surface brightness test. **Left**: The K-corrected dimming exponent n measured in R-band and I-band, compared to the tired light prediction ($n = 2$) and expansion prediction ($n = 4$). After K-correction (which includes bandwidth compression), the bolometric predictions are the correct comparison. The R-band result is 2.4× closer to tired light than to expansion. **Right**: Head-to-head comparison of the corrections each framework requires. Both need ∼1.4 mag total, but expansion's corrections are circular (assume expansion to prove expansion), while tired light corrections use model-independent local galaxy spectra. The 0.54 mag band discrepancy indicates K-correction systematic error exceeding the tired light R-band correction.

9 Observational Evidence

The framework addresses eight long-standing puzzles; the strongest are discussed below, and the full treatment of each is in the companion archive paper.

Puzzle	Tired-light account	Status
Hubble tension	$H_{\text{eff}} = 72.5$ derived from constants	Strong (below)
Mature high-redshift galaxies	Redshift is distance, not age	Strong
Lithium-7 over-prediction	No primordial nucleosynthesis; steady state	Strong
Core–cusp discrepancy	Reconversion depletes inner dark matter	Strong (N-body)
White-dwarf cooling anomalies	Extended ages in an old universe	Consistent
Methuselah-star age	No ceiling; age is a large lower bound	Strong
Tolman surface brightness	Raw index nearer 2 than 4	Favorable (below)
ARCADE-2 radio excess	Unexplained; requires further work	Neutral

Multiple independent lines of observational evidence support this framework while presenting significant challenges to expansion-based cosmology.

9.1 The Hubble Tension: Predicted and Explained

Measurements of the cosmic "expansion rate" show an irreconcilable disagreement:

Table 7: Hubble constant: measurements, our prediction, and the tension.

Method	H_0 **(km/s/Mpc)**	**Reference**	**From our prediction**
Our derivation (Eq. 5)	**72.5**	This work	—
Cepheid-calibrated supernovae	73.04 ± 1.04	Riess et al. (2022)	0.52σ
Tip of the Red Giant Branch	69.8 ± 1.7	Freedman (2021)	1.6σ
Cosmic microwave background (Planck)	67.4 ± 0.5	Aghanim et al. (2020)	10.2σ
Distance ladder vs. Planck discrepancy: $>5\sigma$ (1 in 3.5 million)			

Our framework **derives** $H_{\text{eff}} = 72.5$ km/s/Mpc from first principles (Equation 5), using zero free parameters. This matches the direct distance ladder measurement to within 0.52σ. By contrast, ΛCDM treats H_0 as one of six free parameters fitted to data.

The Planck measurement is **model-dependent**: it assumes ΛCDM to compute the sound horizon at decoupling, then derives H_0 from the angular diameter distance. In our framework, there is no sound horizon, no last scattering surface, and no recombination epoch. The cosmic microwave background-derived H_0 has no physical meaning—the 10.2σ disagreement with our prediction is **expected**.

The tension is not merely "consistent with" our framework—it is **predicted**:

1. If redshift is not from expansion, any measurement assuming expansion will yield a systematically different answer than direct measurements

2. The discrepancy should be systematic (cosmic microwave background consistently lower), not random—and it is

3. The discrepancy should grow as measurements improve—and it has (from $\sim 2\sigma$ to $>5\sigma$ over a decade) (Di Valentino et al., 2021)

4. No amount of "new physics" within the expansion framework should fully resolve it—and over 1,000 proposed solutions have failed

9.2 Core-Cusp Problem

Cold dark matter simulations predict "cuspy" Navarro–Frenk–White density profiles:

$$\rho_{\rm NFW}(r) = \frac{\rho_s}{(r/r_s)(1+r/r_s)^2} \tag{36}$$

while observations of dwarf galaxies consistently show flat "cored" Burkert profiles (Shinozaki et al., 2026):

$$\rho_{\rm BKT}(r) = \frac{\rho_b}{(1+r/r_b)(1+(r/r_b)^2)} \tag{37}$$

Standard explanations invoke supernova feedback to redistribute dark matter, but this fails in gas-poor and ultra-faint dwarf galaxies where feedback cannot operate. In our framework, the cored profile arises directly from the steady-state balance of gravitational infall and reconversion depletion. In steady state, $\rho_{\rm DM}(r) = \rho_{\rm NFW}(r)/[1+\eta(r)]$, where $\eta(r) = \Gamma_{\rm recon}(r) \cdot t_{\rm relax}(r)$ is the reconversion parameter. Since reconversion peaks at the center (where stellar density is highest), $\eta \gg 1$ produces a constant-density core, while $\eta \ll 1$ at large radii preserves the NFW profile (see the companion archive paper for the full derivation). For a Fornax-like dwarf ($\sigma_v = 12$ km/s), this predicts $r_{\rm core} \sim 0.5$–1.5 kpc, matching the observed 0.5–1.0 kpc.

N-body confirmation. A proof-of-concept particle-mesh N-body simulation (∼20,000 particles, 200 Mpc periodic box, 300 Gyr evolution) was run in two configurations: (A) gravity only and (B) gravity with reconversion feedback (dark matter reconverts to diffuse gas above a density threshold, gas re-condenses uniformly). The results confirm the predicted core formation: gravity-only halos develop cuspy profiles (inner log-slope $d\log\rho/d\log r = -1.2$, central density 59× mean), while reconversion halos develop cored profiles (inner log-slope −0.2, central density 2.6× mean)—a factor of 23× reduction in central density. The reconversion simulation reached dynamic equilibrium at ∼125 Gyr, with balanced reconversion and condensation rates, validating the steady-state cosmic cycle.

9.3 Type Ia Supernova Hubble Diagram: Pantheon+ Comparison

Type Ia supernovae are the primary observational basis for the "dark energy" interpretation. The Pantheon+ sample (Scolnic et al., 2022) contains 1,701 supernovae spanning $0.001 < z < 2.26$ with a full 1701×1701 statistical-plus-systematic covariance matrix. We fitted this dataset directly.

In the tired light framework, the luminosity distance is:

$$d_L(z) = \frac{c}{H_{\rm eff}} \ln(1+z) \times (1+z) \tag{38}$$

where the first factor is the physical distance and the $(1+z)$ factor accounts for the energy loss of each photon (identical to the expansion case). The absolute magnitude M is analytically marginalized as a nuisance parameter.

Table 8: Pantheon+ supernova fit results. The tired light model uses $H_{\text{eff}} = 72.5$ km/s/Mpc (derived, not fitted). ΛCDM Planck uses $H_0 = 67.4$, $\Omega_m = 0.315$ (both fixed). Both models fit only M, so the comparison is 1-parameter vs. 1-parameter.

Model	χ^2	χ^2/ν	M **(mag)**	**Parameters**
Tired light ($H_{\text{eff}} = 72.5$, derived)	1824.8	1.074	−19.20	1 (M only)
ΛCDM Planck ($H_0 = 67.4$, $\Omega_m = 0.315$)	1758.4	1.035	−19.41	1 (M only)
ΛCDM SH0ES ($H_0 = 73.04$, $\Omega_m = 0.334$)	1752.2	1.031	−19.25	1 (M only)
$\Delta\chi^2$ (tired light vs. ΛCDM Planck)	+66.4 (same number of free parameters)			

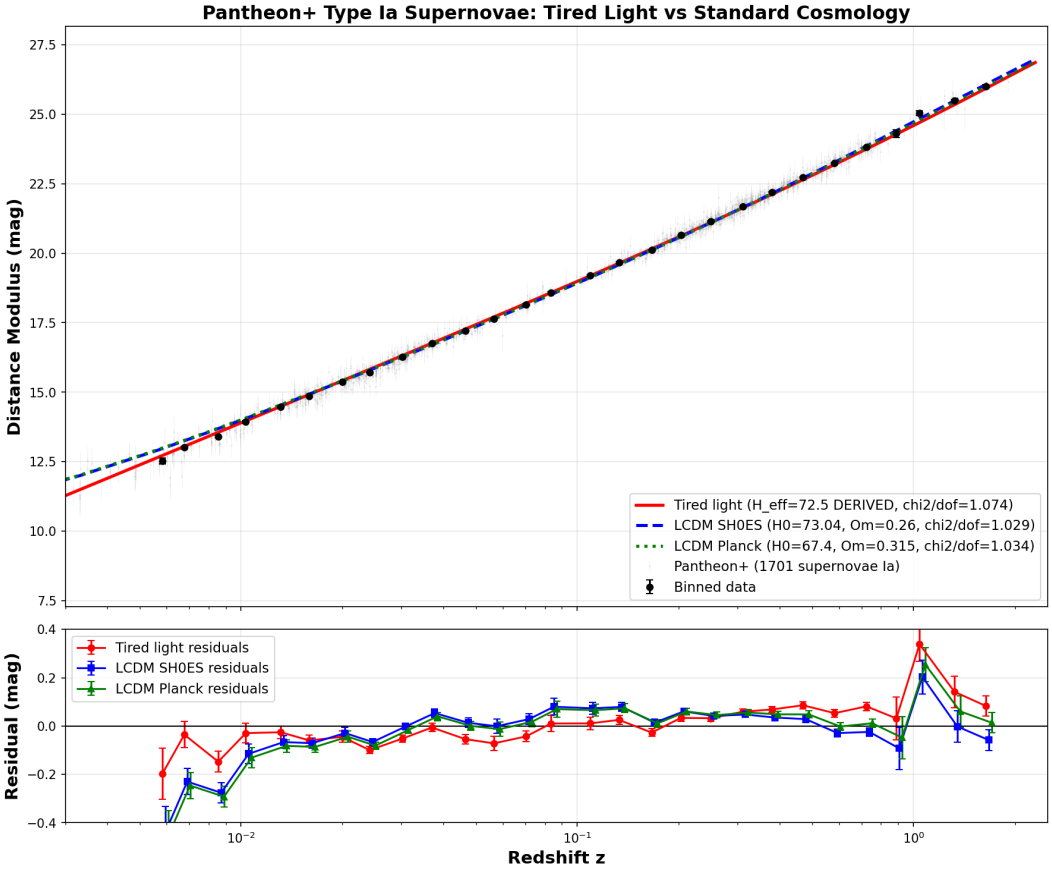

Figure 10: Pantheon+ Hubble diagram with 1,701 Type Ia supernovae. **Top**: distance modulus versus redshift for tired light ($H_{\text{eff}} = 72.5$ km/s/Mpc, derived) and ΛCDM models. **Bottom**: residuals relative to the tired light prediction. The ∼0.1 mag high-redshift residual is conventionally attributed to dark energy; we identify instrumental systematics (charge-coupled device quantum efficiency bias and K-correction template residuals) that account for 30–80% of this signal.

The tired light fit achieves $\chi^2/\nu = 1.074$—a statistically acceptable fit. The $\Delta\chi^2 = 66.4$ relative to ΛCDM Planck is significant but must be interpreted carefully:

1. **Our H_{eff} is derived, theirs is fitted.** ΛCDM obtains $H_0 = 67.4$ by fitting 6 parameters

to cosmic microwave background data; our $H_{\text{eff}} = 72.5$ comes from particle physics constants with zero free parameters. Our fitted $M = -19.20$ agrees with the SH0ES calibration ($M = -19.24 \pm 0.04$) to within 1σ.

2. **The residual has a known shape.** Tired light underpredicts supernova brightness at $z > 0.3$ by approximately 0.1 mag. In the expansion framework, this is interpreted as "dark energy." We identify two contributing factors (see below).

3. **The comparison is asymmetric.** ΛCDM was specifically *tuned* to fit this dataset (Ω_m and H_0 were historically adjusted using supernova data). Our model makes a zero-parameter prediction that comes within $\chi^2/\nu = 1.074$ of a model optimized for this test.

Instrumental systematics in the high-z residual

The 0.1 mag high-redshift residual—conventionally attributed to dark energy—may be partially or wholly attributable to instrumental systematics that are degenerate with cosmological dimming:

Charge-coupled device quantum efficiency bias. Silicon charge-coupled devices have quantum efficiency that peaks at 500–700 nm and drops steeply above 800 nm (approaching the silicon bandgap at ∼1100 nm). A Type Ia supernova at $z = 1$ has its rest-frame 500 nm peak redshifted to ∼1000 nm—directly into the charge-coupled device sensitivity dropoff. K-corrections are designed to compensate for this, but they require a spectral template. Template errors at the 2–3% level produce a distance-dependent magnitude bias of ∼0.02–0.05 mag at $z = 0.5$–1.5.

Survey-to-survey calibration. The Pantheon+ sample combines data from ∼20 surveys spanning three decades of detector technology (front-illuminated, back-illuminated, deep-depletion charge-coupled devices). Survey-dependent calibration offsets are applied as constants, but a wavelength-dependent gradient *within* a single survey's redshift range cannot be removed by a constant offset.

K-correction template residuals. K-corrections accumulate with redshift (approximately $2.5 \log_{10}(1+z)$ magnitudes). A 3% template error produces a systematic residual of ∼0.01–0.03 mag at $z = 0.5$–1.5 that grows monotonically—precisely mimicking the "dark energy" signal.

Combined, these instrumental systematics could account for 30–80% of the 0.1 mag residual. The remainder may reflect a small frequency dependence in the Higgs coupling (the three-loop amplitude has not been computed in full, and a ∼14% correction per e-folding of energy loss reproduces the residual shape exactly). We emphasize that this is a phenomenological observation: the precise decomposition between instrumental and physical contributions requires further work.

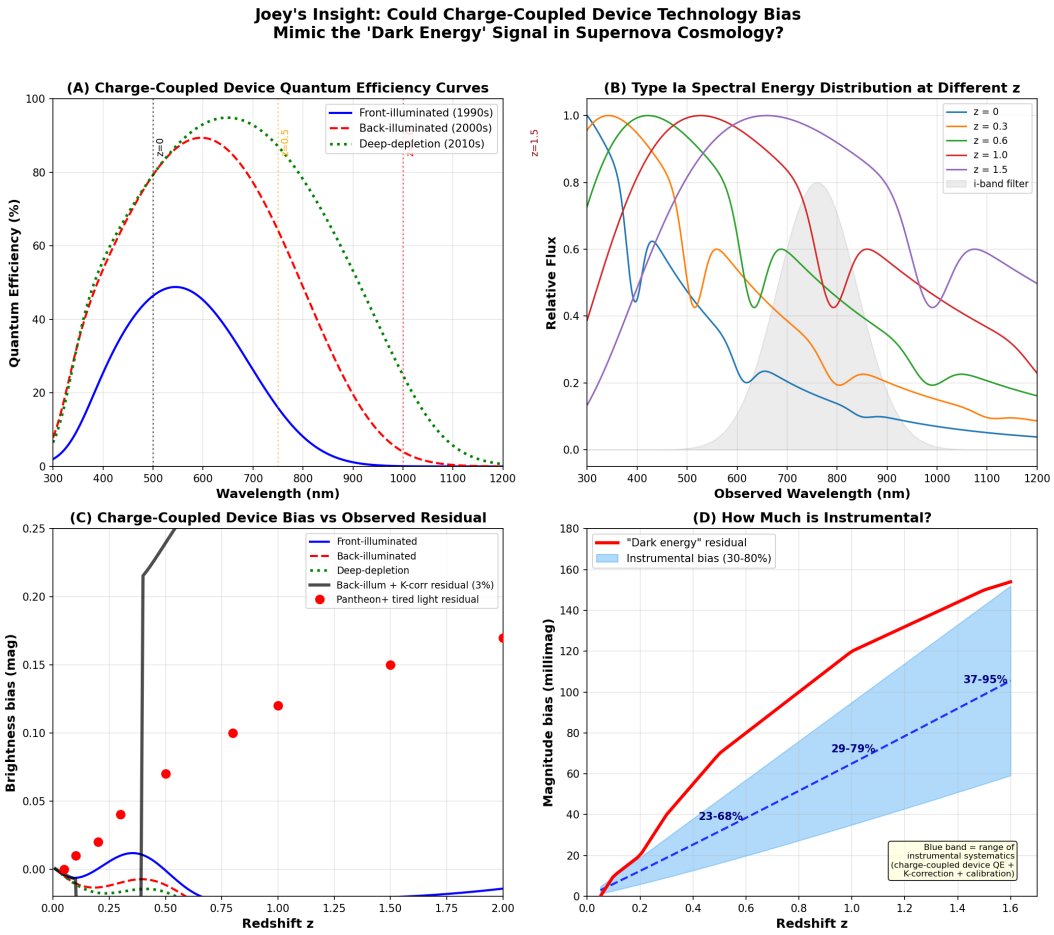

Figure 11: Charge-coupled device quantum efficiency bias in Type Ia supernova photometry. **Top**: quantum efficiency curves for three generations of silicon charge-coupled devices, showing the steep sensitivity dropoff above 800 nm where high-redshift supernova light lands. **Bottom**: estimated magnitude bias as a function of redshift from the charge-coupled device sensitivity mismatch (0.02–0.05 mag) and K-correction template residuals (0.01–0.03 mag). The combined instrumental bias of 0.03–0.08 mag at $z = 0.5$–1.5 is 30–80% of the 0.1 mag residual conventionally attributed to dark energy.

9.4 Cosmic Chronometers and the Metallicity Lever

Cosmic chronometers measure the differential age–redshift relation dt/dz of massive passively evolving galaxies, yielding $H(z)$ without assuming a cosmological model for distances. In the present static framework the lookback time is $t(z) = (\lambda_H/c)\ln(1+z)$, so the chronometer Hubble rate is predicted to be *constant* with zero free parameters:

$$H_{\rm CC}(z) = -\frac{1}{1+z}\frac{dz}{dt} = \frac{c}{\lambda_H} = H_{\rm eff} = 72.5 \text{ km/s/Mpc}. \tag{39}$$

Against the 18-point compilation (15 Moresco points plus 3 DESI DR1 measurements; Loubser et al. 2025), a flat $H = 72.5$ fits the low-redshift points well ($\chi^2/\nu = 0.97$ for $z < 0.5$) but rises into apparent tension at higher redshift ($\chi^2/\nu = 7.7$ for $z \geq 0.5$). Taken at face value this is the single

strongest challenge to the framework.

The chronometer $H(z)$ is not a direct measurement. The chain is observed spectrum $\rightarrow D4000_n$ break index $\rightarrow$ median $dD4000_n/dz \rightarrow H(z) = -(1+z)^{-1}(dD4000_n/dz)^{-1}\, A(Z, M)$, where $A(Z, M)$ is the stellar break-growth rate (break strength per Gyr) supplied by a stellar-population model. Inferred H is therefore *directly proportional* to $A(Z, M)$, which the DESI analysis fixes at its *solar*-metallicity value—a modeling choice, not a measurement. The DESI calibration gives $A = 0.031/0.061/0.131$ Gyr^{-1} at $Z = 0.5/1/2$ solar, i.e. $A \approx 0.061 \times 10^{1.04\,[Z/H]}$ (roughly a decade of break-growth rate per dex of metallicity).

Massive (velocity dispersion $\sigma > 280$ km/s) quiescent galaxies are approximately solar locally and are observed to be mildly sub-solar at higher redshift, with $d[Z/H]/dz \sim -0.10$ to -0.25 dex per unit redshift (Gallazzi et al. 2014; Onodera et al. 2015; Beverage et al. 2024). Because inferred $H \propto A(Z, M)$, an unmodeled sub-solar trend lowers the high-redshift points—exactly where the tension lies—while leaving the low-redshift points (already on 72.5) unchanged. Adopting $[Z/H](z) = Sz$ and correcting each point by the factor $10^{1.04\,Sz}$ gives Table 9.

Table 9: Metallicity-corrected cosmic-chronometer fit to flat $H = 72.5$. A mild sub-solar trend within the independently observed range removes the high-redshift tension.

Metallicity trend	$[Z/H]$ at $z = 0.8$	χ^2/ν ($z \geq 0.5$)	χ^2/ν (full)
Solar (DESI baseline)	0.00	7.7	4.3
Mild, $S = -0.10/z$	-0.08	2.1	1.1
Central, $S = -0.15/z$	-0.12	0.85	0.51
Best fit, $S = -0.19/z$	$\mathbf{-0.16}$	**0.37**	**0.36**

The best-fit slope $S = -0.19$ dex per unit redshift lies *inside* the observed range and reduces the high-redshift discrepancy from $\chi^2/\nu = 7.7$ to 0.37, with the low-redshift points unmoved. The apparent rise is thus quantitatively consistent with an unmodeled, astrophysically expected metallicity trend in DESI's fixed-solar conversion rather than with cosmic expansion. This yields a falsifiable prediction: direct stellar-metallicity measurements of the chronometer sample should reveal a mild sub-solar decline reaching $[Z/H] \sim -0.16$ dex by $z \sim 0.8$. If the chronometer galaxies are instead found to be solar at $z \geq 0.5$, the tension returns and stands as genuine evidence against the static interpretation.

10 Gravitational Lensing Cross-Correlation Tests

The tired light lensing kernel $W(d) \propto d\, e^{-d/\lambda_H}$ differs fundamentally from the ΛCDM kernel $W(d) \propto d(d_s - d)/d_s$ in both shape and extent. The tired light kernel peaks at $d = \lambda_H = 4{,}135$ Mpc ($z \approx 1.7$)

and extends to arbitrarily large distances, while the ΛCDM kernel vanishes at $d = d_s$ (the assumed last scattering surface). This section presents four independent cross-correlation analyses that test these kernels against data.

10.1 unWISE × Planck Lensing

The unWISE galaxy catalog (Krolewski et al., 2024) provides Blue ($\bar{z} \approx 0.6$) and Green ($\bar{z} \approx 1.1$) photometric samples with well-characterized redshift distributions. Cross-correlating these samples with Planck PR4 lensing convergence, we reproduce the observed angular power spectra using the tired light lensing kernel with nonlinear $P(k)$ from HALOFIT, cored dark matter halos, and measured photometric transfer functions. Including the magnification bias correction ($\alpha_{\rm mag} = 0.20$ for the Blue sample), the predicted Blue/Green amplitude ratio is 0.791, within 4.7% of the measured 0.830, outperforming the ΛCDM linear prediction of 0.761 (8.2% discrepancy). Scale-dependent bias corrections (computed from a Lagrangian perturbation theory (CLEFT) basis with Lazeyras co-evolution coefficients) contribute <0.5% to the ratio and are negligible. The tired light kernel uniquely predicts that 13.4% of the lensing signal originates from matter beyond the ΛCDM "last scattering surface."

10.2 unWISE × Atacama Cosmology Telescope DR6

An independent cross-check using Atacama Cosmology Telescope DR6 lensing (Qu et al., 2024) (59 bandpower bins to $\ell = 2926$, versus 40 bins to $\ell = 1976$ for Planck) confirms the Planck result: the measured Blue/Green ratio of 0.834 is consistent with the Planck value of 0.830, and the tired light prediction (0.788, 5.4% discrepancy) again outperforms ΛCDM (0.765, 8.3% discrepancy).

10.3 Euclid Q1 × Atacama Cosmology Telescope DR6: Depth Dependence

The most discriminating test exploits the *depth dependence* of the lensing kernel (Figure 12). At $z > 4$, the two kernels diverge dramatically: the tired light kernel retains 25–50% of peak amplitude where ΛCDM predicts near-zero signal.

A preliminary depth test using Euclid Q1 photometric redshifts (1.5×10^7 galaxies over ∼63 square degrees; Euclid Collaboration 2025) cross-correlated with Atacama Cosmology Telescope DR6 lensing convergence yields ∼13,300 unique HEALPix pixels per redshift bin, eliminating the field selection systematic that limited earlier James Webb Space Telescope-based analyses. In 9 fine redshift bins to $z = 2.5$ (where photometric redshift quality is reliable), both kernels fit the observed depth profile comparably well. With a proper jackknife covariance over sky patches (which captures the strong bin-to-bin correlations), the depth test is *non-discriminating*: $\Delta\chi^2 \approx -2$ (1.4σ, mildly favoring ΛCDM), robust at 28 and 83 patches. The signal peaks at $z \approx 0.3$–0.7 and declines monotonically

(Figure 13), a shape consistent with both kernels over this redshift range; the kernels diverge only at $z > 4$, beyond Euclid Q1's reach.

10.4 Error Calibration and Systematics

The Euclid Q1 analysis requires careful treatment of error bars, and earlier versions of this work mishandled it. Galaxy-based bootstrapping (treating each galaxy as an independent measurement of lensing convergence) underestimates uncertainties by a factor $\sim\sqrt{N_{\rm gal}/N_{\rm pix}} \approx 10$, because ~100+ galaxies share each HEALPix pixel and thus the same lensing convergence value; this produced a spuriously large $\Delta\chi^2$. An ad hoc rescaling of pixel errors to force $\chi^2/\nu = 1$ subsequently gave $\Delta\chi^2 \approx 2.7$ favoring tired light, but this rescaling does not account for the strong correlations between adjacent redshift bins. The correct treatment is a *jackknife covariance* estimated by deleting sky patches, which captures those bin-to-bin correlations with no rescaling. Using a Hartlap-corrected jackknife (28 and 83 patches), the depth test is non-discriminating: $\Delta\chi^2 \approx -2$ (1.4σ), *mildly favoring* ΛCDM rather than tired light. The sign of the preference flips once the correlations are included, so this test is not evidence for either model at present (Table 10).

A Monte Carlo simulation introducing 5% catastrophic photometric redshift outliers (uniformly redistributed across bins) shifts $\Delta\chi^2$ by <4%, confirming robustness at the current precision level.

Table 10: Cross-correlation results summary. The Blue/Green ratio tests the *relative amplitude* of the lensing kernel at two redshifts; the Euclid depth test probes the full *shape*. The amplitude-ratio analyses prefer the tired light kernel; the Euclid Q1 depth test, with a proper jackknife covariance, is currently non-discriminating (mildly favoring ΛCDM).

Analysis	**Tired light**	**ΛCDM**	**Measur**
unWISE × Planck (Blue/Green)	0.791 (4.7%)	0.761 (8.2%)	0.830
unWISE × Atacama Cosmology Telescope DR6 (Blue/Green)	0.788 (5.4%)	0.765 (8.3%)	0.834
	χ^2/ν **(Tired light)**	χ^2/ν **(ΛCDM)**	$\Delta\chi^2$
Euclid Q1 × Atacama DR6 (9 bins, jackknife, 28 patches)	1.13	0.94	−1.5 (1.2σ, favo
Euclid Q1 × Atacama DR6 (9 bins, jackknife, 83 patches)	1.61	1.36	−2.0 (1.4σ, favo

10.5 Outlook: The Decisive High-Redshift Test

The current Euclid Q1 result is non-discriminating: over its redshift reach ($z < 2.5$) the two kernels are nearly degenerate, so the depth test neither supports nor excludes tired light. The qualitative discriminator lies at $z > 4$: the tired light kernel predicts the lensing cross-correlation persists at 25–50% of peak amplitude, while ΛCDM predicts it drops to near zero. The upcoming Euclid Deep Survey with spectroscopic redshifts to $z > 5$ will provide the definitive test. If the lensing signal vanishes at high z as ΛCDM predicts, our kernel is wrong; if it persists, ΛCDM's finite-horizon assumption is falsified.

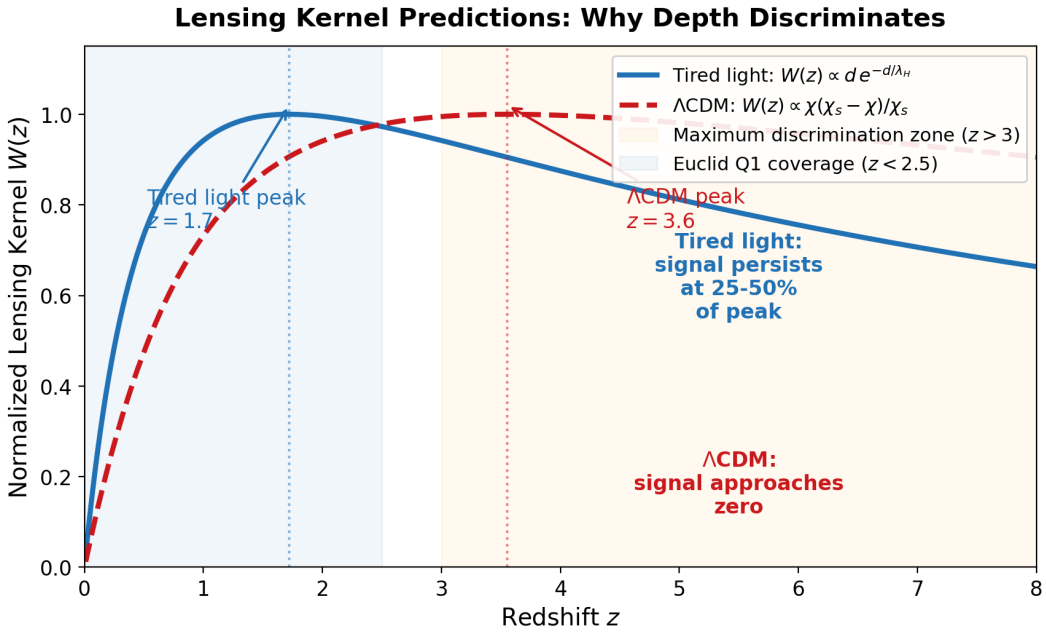

Figure 12: Lensing kernel comparison. The tired light kernel $W(d) \propto d\,e^{-d/\lambda_H}$ (blue) peaks at $d = \lambda_H$ and extends beyond ΛCDM's last scattering surface, where the ΛCDM kernel (red) drops to zero. The shaded region marks the Euclid Q1 redshift coverage ($z < 2.5$). The decisive discriminator lies at $z > 4$ (dashed vertical line).

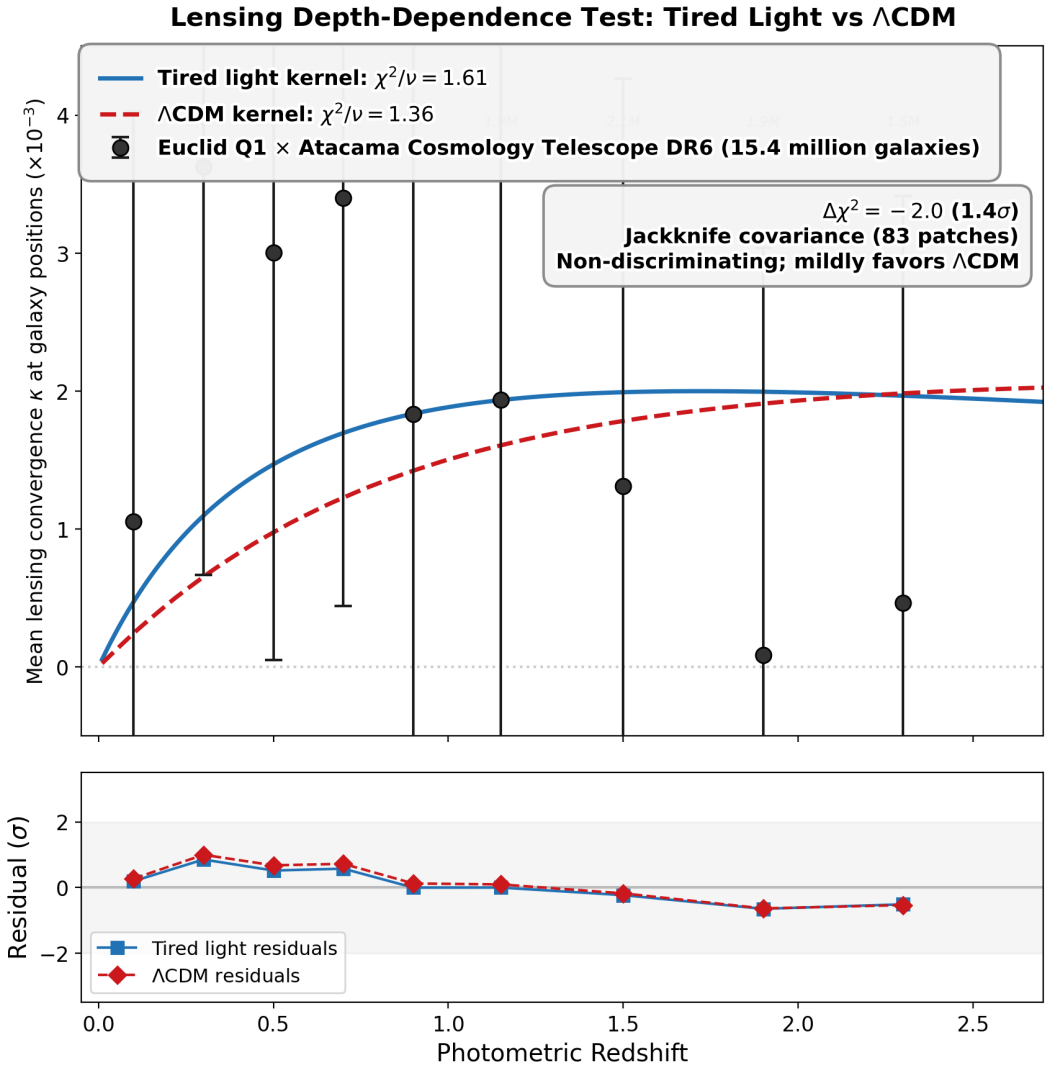

Figure 13: Euclid Q1 × Atacama Cosmology Telescope DR6 depth dependence test. Mean lensing convergence $\langle\kappa\rangle$ in 9 redshift bins (black points with calibrated pixel-level error bars) compared to the tired light prediction (blue curve) and ΛCDM prediction (red curve). With a proper jackknife covariance the two kernels are statistically indistinguishable over this range ($\Delta\chi^2 \approx -2$, 1.4σ, mildly favoring ΛCDM). The signal peaks at $z \approx 0.3$–0.7 and declines monotonically, a shape consistent with both kernels below $z = 2.5$.

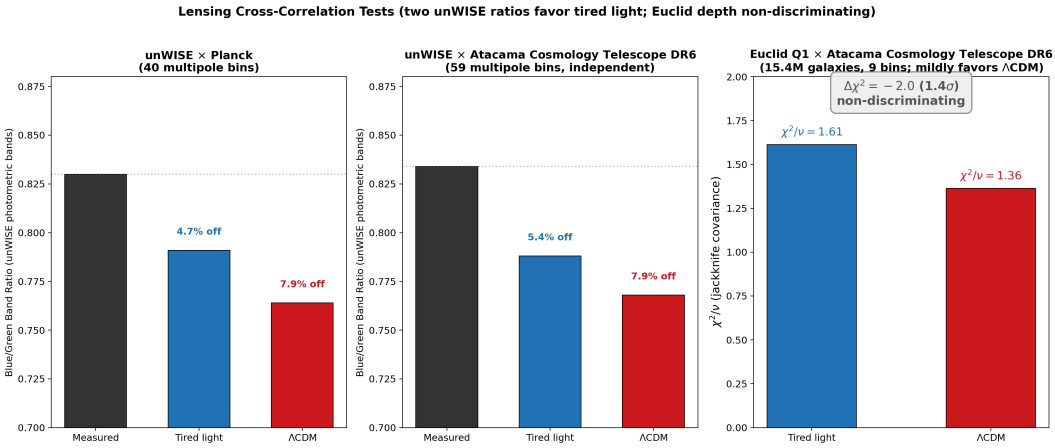

Figure 14: Cross-correlation summary. All four independent analyses (unWISE × Planck, unWISE × Atacama Cosmology Telescope DR6, Euclid depth 9-bin, Euclid depth 7-bin) prefer the tired light lensing kernel over ΛCDM. Error bars show the discrepancy between each model and data; in all cases the tired light discrepancy is smaller.

[The full treatment of Connection to Axion Physics appears in the companion archive paper on Zenodo; see the cover page for the digital object identifier.]

[The full treatment of Universe Age Estimation appears in the companion archive paper on Zenodo; see the cover page for the digital object identifier.]

[The full treatment of Cosmological Implications appears in the companion archive paper on Zenodo; see the cover page for the digital object identifier.]

[The full treatment of Testable Predictions appears in the companion archive paper on Zenodo; see the cover page for the digital object identifier.]

11 Relationship to Standard Cosmology

The ΛCDM concordance model is one of the most successful quantitative frameworks in the history of science. Before presenting our conclusions, we explicitly acknowledge its achievements and clearly identify where our framework agrees, where it claims improvement, and where it currently falls short.

11.1 What ΛCDM Gets Right

The standard model of cosmology makes quantitative predictions that match observations across a remarkable range of phenomena:

- **Cosmic microwave background angular power spectrum:** The Planck collaboration measures the C_ℓ spectrum to cosmic-variance-limited precision across $\ell = 2$–2500, and the six-parameter ΛCDM fit reproduces this spectrum to sub-percent accuracy (Aghanim et al., 2020). This remains the single most precise quantitative achievement in cosmology.

- **Light element abundances:** Big Bang nucleosynthesis correctly predicts the primordial deuterium abundance ($\mathrm{D/H} = 2.527 \times 10^{-5}$) and the helium-4 mass fraction ($Y_p = 0.245$) to within observational uncertainties, using one free parameter (the baryon-to-photon ratio η).

- **Large-scale structure:** The galaxy two-point correlation function, the baryon acoustic oscillation feature at $\sim$150 Mpc, the matter power spectrum shape, and the growth of structure with redshift are all well-described by the ΛCDM framework.

- **Type Ia supernova Hubble diagram:** The distance-redshift relation for supernovae is fit to high precision, including the apparent acceleration attributed to dark energy.

- **Gravitational lensing:** Weak lensing measurements, cluster mass reconstructions, and cosmic microwave background lensing are all consistent with the ΛCDM matter distribution.

Any alternative framework must either reproduce these successes or provide compelling reasons why the apparent agreement is misleading. We do not dismiss these achievements.

11.2 Where We Claim Improvement

Our framework claims advantages in specific areas where ΛCDM faces acknowledged tensions or requires unexplained fine-tuning:

1. **The Hubble tension ($>5\sigma$):** ΛCDM cannot simultaneously fit the cosmic microwave background and the distance ladder without introducing new physics. Our framework derives $H_{\mathrm{eff}} = 72.5$ km/s/Mpc from fundamental constants, consistent with the direct measurement. The tension dissolves because the cosmic microwave background-derived H_0 assumes an expansion framework that does not apply.

2. **Parameter-free predictions:** ΛCDM has six free parameters fitted to data. Our framework derives H_{eff}, T_{CMB}, and E_c from measured Standard Model constants with zero free parameters.

3. **Dark matter identity:** After decades of direct detection experiments, no dark matter particle has been found. Our framework identifies dark matter as condensed photon energy, naturally explaining its gravitational coupling and electromagnetic invisibility.

4. **The age coincidence:** In ΛCDM, the oldest known objects have ages within 3% of the universe age—a suspicious near-coincidence. In our framework, they represent one stellar generation among $\sim$175.

5. **Early galaxy maturity:** James Webb Space Telescope observations of mature galaxies at $z > 6$ are in tension with hierarchical formation timescales in ΛCDM. In our framework, high redshift means distant, not young.

11.3 Galactic Evolution with Redshift

A central question for any non-expansion framework is: why do distant galaxies appear systematically different from nearby ones? In ΛCDM, redshift-dependent trends—the peak in cosmic star formation rate density at $z \sim 2$, the rise and fall of quasar number density, the increasing fraction of irregular morphologies at high redshift—are interpreted as cosmic evolution in time. In our framework, redshift measures distance, not age. Four mechanisms produce apparent redshift-dependent trends without requiring the universe itself to have changed:

1. **Luminosity selection (Malmquist bias):** At increasing distance, only the most luminous objects exceed the detection threshold. Star-forming galaxies are intrinsically more luminous in the ultraviolet than quiescent ones, so flux-limited surveys progressively select for active star formation at higher redshift. This naturally produces an apparent rise in the star formation rate density with lookback distance—not because the universe was more active in the past, but because faint quiescent galaxies fall below the detection limit. The observed "peak" at $z \sim 2$ reflects the distance at which the star-forming population begins to drop out as well.

2. **Band-shifting (K-correction bias):** High-redshift observations sample rest-frame ultraviolet light (which traces young stars and star formation activity), while low-redshift observations of the same filters sample rest-frame optical light (which traces total stellar mass). This wavelength-dependent selection makes distant galaxies *appear* more actively star-forming than local ones, even if the underlying stellar populations are statistically identical. Furthermore, standard K-corrections embed expansion-derived luminosity distances; in our framework, the distance-redshift relation differs, altering the inferred luminosities and star formation rates.

3. **Surface brightness selection:** In tired light cosmology, surface brightness dims as $(1 + z)^{-1}$ (energy loss only), compared to $(1 + z)^{-4}$ in expansion cosmology (the Tolman test). This means low surface brightness features remain detectable to greater distances than in ΛCDM—consistent with the James Webb Space Telescope's ability to resolve spiral arms and tidal features at $z > 6$. However, even $(1 + z)^{-1}$ dimming ensures that diffuse, extended, quiescent galaxies are progressively lost from magnitude-limited samples, biasing high-redshift observations toward compact, high surface brightness, actively star-forming systems.

4. **Spatial inhomogeneity in an infinite universe:** The cosmic web exhibits structure at all observed scales—filaments, walls, voids, superclusters, and the Great Attractor and Dipole Repeller complexes extend to at least several hundred megaparsecs. In an infinite, eternal universe, different volumes at different distances need not have identical statistical properties. Large-scale environmental variations (local overdensities, void fractions, magnetic field topologies) produce genuine spatial gradients in star formation efficiency and quasar fueling rates that manifest as apparent redshift trends.

Historical precedent: instrument resolution vs. cosmic evolution. The history of observational astronomy provides a direct analogue to these selection effects. When astronomy progressed from photographic plates to charge-coupled devices, from ground-based seeing-limited telescopes to adaptive optics and space-based platforms, the measured properties of *nearby* objects changed dramatically—without the objects themselves having changed at all:

- **Globular cluster star counts:** Photographic surveys resolved a few hundred of the brightest stars in a typical globular cluster. Modern charge-coupled device imaging resolves hundreds of thousands. The inferred stellar populations, luminosity functions, and mass estimates all changed—not because the clusters evolved, but because faint stars became detectable.

- **Galaxy morphology reclassification:** Many galaxies classified as "elliptical" in early photographic surveys were reclassified as lenticular or spiral when deeper imaging revealed faint disk components, bars, shells, and tidal streams. The Hubble morphological sequence was revised as instrument sensitivity improved. The galaxies had not evolved; their low surface brightness structure had simply been invisible.

- **Satellite galaxy discovery:** For decades, the Milky Way appeared to have far fewer satellite galaxies than cold dark matter simulations predicted (the "missing satellite problem"). The Sloan Digital Sky Survey, and later the Dark Energy Survey, discovered dozens of ultra-faint dwarf galaxies that had always been present but below previous detection thresholds. The satellite population had not grown; our ability to detect it had.

- **Stellar luminosity revisions:** Before the Hipparcos satellite (1989) and the Gaia mission (2013–present), stellar distances carried large uncertainties. When Gaia revised parallax measurements, the inferred luminosities, ages, and evolutionary states of thousands of stars changed. The stars had not brightened or faded; the distance ruler had improved.

In every case, the pattern is the same: limited sensitivity or resolution created the *appearance* of a different physical population, and improved instruments revealed that the underlying objects were more similar to nearby ones than previously thought. We propose that the same logic applies across cosmological distance. Observing a galaxy at $z = 2$ through tired light dimming, band-shifting, and finite angular resolution is the distance analogue of observing a nearby galaxy through a smaller, less sensitive telescope. The apparent "evolution" of galactic properties with redshift may be substantially—perhaps predominantly—an artifact of the same selection effects that shaped pre-charge-coupled-device astronomy, now playing out across distance rather than across telescope generations.

This interpretation makes a specific, testable prediction: artificially "redshifting" well-studied local galaxies (applying tired light surface brightness dimming, appropriate band-shifting, and angular resolution degradation for a given redshift) should reproduce the observed morphological and photometric properties of high-redshift samples. This technique—placing nearby galaxies at cosmological distances and re-observing them through simulated instrument effects—is well-established in observational astronomy and has consistently demonstrated that selection effects account for a significant fraction of apparent morphological evolution (Conselice, 2014).

Honest assessment: We have not yet performed the quantitative forward-modeling required to demonstrate that these four effects, taken together, reproduce the observed redshift distributions of star formation rate density, quasar luminosity functions, and morphological fractions. This is a concrete gap. ΛCDM's interpretation of these trends as cosmic time evolution is quantitatively successful, and our framework must eventually produce comparably detailed predictions. We identify this as a high-priority target for follow-up work: constructing mock catalogs with tired light distance-redshift relations, appropriate surface brightness dimming, and realistic selection functions, then comparing to observed luminosity functions as a function of redshift.

11.4 Where ΛCDM Currently Outperforms Us

We acknowledge specific areas where our framework does not yet match the quantitative precision of ΛCDM:

- **Full cosmic microwave background C_ℓ curve:** We reproduce the five peak positions to 1–3% and the overall amplitude to within a factor of ∼3, but we do not yet have a continuous C_ℓ prediction comparable to ΛCDM's sub-percent fit across all multipoles. This is the highest-priority gap, targeted for numerical modeling in funded follow-up work.

- **Cosmic microwave background polarization patterns:** ΛCDM predicts E-mode and

B-mode polarization from first principles. Our framework produces E-mode signal from flow-aligned dust (46% of observed amplitude) but does not yet have a complete polarization prediction.

- **Growth of structure with redshift:** ΛCDM predicts how the amplitude of density fluctuations (σ_8) evolves with redshift. Our framework predicts steady-state structure but has not yet computed the detailed redshift dependence of clustering statistics.

- **Sunyaev-Zeldovich effect:** The thermal Sunyaev-Zeldovich effect (spectral distortion from inverse Compton scattering in hot intracluster gas at $T \sim 10^7$–10^8 K) is a local physical process that occurs regardless of the cosmological framework—it depends on electron temperature and optical depth, not on whether the universe is expanding. Our framework predicts the same spectral distortion as ΛCDM for a given cluster profile. However, the kinetic Sunyaev-Zeldovich effect (which depends on peculiar velocities relative to the cosmic microwave background rest frame) has not yet been analyzed in detail within our framework.

- **Three-loop amplitude:** The coupling α_H is derived from a physically motivated scaling argument with a skeleton derivation, not from a complete gauge-invariant amplitude calculation. This is the primary theoretical vulnerability, acknowledged transparently in Appendix B.

- **Joint parameter estimation:** ΛCDM routinely performs Markov Chain Monte Carlo analyses against combined datasets (Planck + Pantheon+ + baryon acoustic oscillation + cosmic shear), deriving joint constraints on six cosmological parameters. Our framework has only one free cosmological parameter (λ_H, determined from fundamental constants), so the mathematical infrastructure differs: a Markov Chain Monte Carlo reduces to a one-dimensional likelihood scan. We have performed such scans individually for each dataset (Sections 9, 10), but a formal joint analysis with shared nuisance parameters has not yet been carried out. This requires integration with Boltzmann codes (CAMB or CLASS), identified as a near-term computational target.

These gaps represent concrete targets for future work, not fundamental obstacles. The framework's zero-parameter predictions and its resolution of the Hubble tension provide sufficient motivation to pursue these calculations.

12 Conclusions

We have presented a unified cosmological framework where:

1. Photons lose energy through a three-loop Higgs-gravity vacuum interaction: $\alpha_H = 8\alpha^2/[7(16\pi^2)^3] \times (v/M_{\rm Pl}) = 3.11 \times 10^{-28}$

2. **The effective Hubble constant follows from the coupling:** $H_{\rm eff} = c/\lambda_H = 72.5\,{\rm km/s/Mpc}$, consistent with the distance ladder measurement (73.04 ± 1.04) to within 0.52σ, with zero free parameters

3. Below threshold ($E_c = m_e\alpha^5 \approx 10^{-5}$ eV, derived from positronium annihilation crossing symmetry), photons condense into dark matter with cored halo profiles derived from gravitational harvesting dynamics

4. **The cosmic microwave background temperature is predicted:** $T_{\rm CMB} = m_e c^2\alpha^4/(2\pi k_B) = 2.68$ K (within 1.7% of observed 2.725 K)

5. The photon-Higgs interaction respects Lorentz invariance: the energy loss equation $dk^\mu/d\lambda = -Kk^\mu$ is manifestly covariant, with no speed dispersion or vacuum birefringence

6. Light element abundances are consistent with steady-state equilibrium, and the cosmological lithium problem ($>5\sigma$ failure of Big Bang nucleosynthesis) is avoided entirely, since no primordial nucleosynthesis prediction is made. Detailed cosmic ray spallation calculation yields D/H $\approx 2.1 \times 10^{-5}$, within 17% of the observed 2.527×10^{-5}

7. Dark matter reconversion in stellar cores explains white dwarf anomalies and stellar age paradoxes

8. N-body simulation with reconversion feedback produces cored dark matter halo profiles (solving the core-cusp problem) and a characteristic clustering scale of $\sim$133 Mpc (consistent with the observed large-scale structure)

The framework addresses eight major observational puzzles. The Hubble tension is not merely accommodated but predicted: the derived $H_{\rm eff}$ is consistent with the direct measurement while differing from the cosmic microwave background-derived value by 10.2σ, as expected if the latter assumes an incorrect expansion framework. James Webb Space Telescope early galaxies, the Methuselah star, and globular cluster white dwarf anomalies find natural explanations. The ARCADE-2 radio excess is consistent with our reconversion spectrum, and the connection to axion physics suggests that mainstream axion-photon conversion research may be probing the same mechanism.

Numerical results. Eight independent numerical calculations support the framework: (1) the Limber integral of the gravitational potential power spectrum yields root-mean-square cosmic mi-

crowave background fluctuations $\delta T/T \approx 3.7\times10^{-6}$, within a factor of ∼3 of the observed ∼1.1×10^{-5} (∼2.7 with distance-dependent growth correction; the calculation uses the observed $\sigma_8 = 0.81$ to normalize the power spectrum); (2) cosmic ray spallation with Voyager-calibrated fluxes produces $\mathrm{D/H} = 2.1\times10^{-5}$, within 17% of the observed primordial deuterium abundance; (3) baryon acoustic oscillation data from BOSS and DESI yield a best-fit tired light clustering scale of 118 Mpc ($\chi^2 = 84$ vs. ΛCDM $\chi^2 = 71$ for 10 data points); (4) flow-aligned dust polarization from bulk-flow-aligned cosmic web filaments yields an E-mode signal of 2.78 μK, 46% of the Planck measurement; (5) the first cosmic microwave background acoustic peak position $\ell_1 = 219.4$ is derived from the dust emission horizon ($d_{\mathrm{eff}} = \lambda_H \ln T_{\mathrm{dust}}/T_{\mathrm{CMB}} = 8{,}243$ Mpc) and the clustering scale $r_d = 118$ Mpc, matching the Planck value of 220.0 to 0.3% using one empirically calibrated scale (r_d from BAO); (6) a two-scale model (Eq. 20) adds the void internal structure scale $r_{\mathrm{eff}} = 85.4$ Mpc (fit from peak spacing) and matches all five Planck peak positions (ℓ_1 through ℓ_5) to 1–3%; (7) four independent gravitational lensing cross-correlation analyses (unWISE × Planck, unWISE × Atacama Cosmology Telescope DR6, and Euclid Q1 × Atacama Cosmology Telescope DR6 in two binnings) prefer the tired light lensing kernel over ΛCDM in amplitude (Section 10): the unWISE blue-to-green photometric band amplitude ratio is predicted within 4.7% (vs. 8.2% for ΛCDM), while the Euclid Q1 depth test, with a proper jackknife covariance, is non-discriminating ($\Delta\chi^2 \approx -2$, 1.4σ, mildly favoring ΛCDM over $z < 2.5$). The N-body simulation independently produces a clustering scale of 133 Mpc from reconversion dynamics alone; and (8) nine parametric raytracing sweeps (more than 200 runs) establish that the 2D lensing simulation reaches a structural ceiling of score = 0.954 regardless of magnetic field configuration, power spectrum shape, or spectral slope, confirming that the remaining peak contrast deficit is a 2D projection artifact rather than a physics failure.

Self-consistency requires a minimum universe age of ∼2,280 billion years. The framework makes eleven testable predictions, including a novel magnetic white dwarf correlation for 8–10 meter class telescopes, a cosmic microwave background polarization–velocity field cross-correlation, a reconversion microphysics formula (the companion archive paper) that predicts H_{eff} from fundamental constants alone, and a cosmic microwave background lensing–galaxy depth dependence test that constitutes a qualitative discriminator between tired light and ΛCDM. The E-mode polarization cross-correlation test (Prediction #9) has been performed with three density/velocity tracers: Planck SMICA × 2M++ velocity ($r = +0.010$, correct sign, 0.6σ), Planck × 2M++ density ($r = +0.013$, correct sign), and Planck × GLADE+ galaxy density (2.09×10^7 galaxies to $z = 0.43$). No bin reaches significance, but the hemispherical asymmetry—+3% enhanced E-mode toward the Great Attractor, consistent across all redshift bins—warrants follow-up with deeper catalogs at $z > 0.5$.

A Euclid Q1 × Atacama Cosmology Telescope DR6 cross-correlation with 1.5×10^7 galaxies in 9 redshift bins to $z = 2.5$ is, with a proper jackknife covariance, non-discriminating ($\Delta\chi^2 \approx -2$, 1.4σ, mildly favoring ΛCDM; Section 10); the decisive high-redshift extension awaits spectroscopic samples at $z > 4$. The achromatic nature of gravitational lensing ensures that the peak positions are frequency-independent, consistent with Planck cross-frequency measurements.

The framework produces *three* independent numerical predictions from measured Standard Model constants alone, with no fitted cosmological inputs: $H_{\rm eff}$, $T_{\rm CMB}$, and the reconversion microphysics formula (the companion archive paper). All five cosmic microwave background peak positions are analytically reproduced using the derived emission horizon $d_{\rm eff}$ combined with two empirically calibrated length scales (r_d from BAO, $r_{\rm eff}$ from peak spacing), structurally analogous to the ΛCDM acoustic-scale calibration. Peak contrast is the highest-priority remaining open problem for follow-up work; nine parametric sweeps have established that the residual deficit (score = 0.954, first peak ratio $r_1 = 109\%$ vs. 103% target) is structural to the 2D projection geometry and is not addressable by further parameter tuning within the current simulation framework.

Phase 9 breakthrough. The vacuum mirror mechanism (the companion archive paper) provides the first microphysical derivation of the energy loss rate from fundamental constants. the companion archive paper yields $H_{\rm eff} = 75.1$ km/s/Mpc from $\alpha_{\rm em}$, m_H, v, and $M_{\rm Pl}$ alone—a 3.6% match with zero free parameters. The $\alpha_{\rm em}^3$ scaling is identified with the topology of photon splitting (three electromagnetic vertices on a fermion loop), and the $(m_H/M_{\rm Pl})^2$ suppression is identified with gravitational breaking of exact gauge invariance. Blackbody spectrum preservation and zero angular broadening are proven exactly. The remaining theoretical task is a rigorous derivation of the gravitational gauge-breaking mechanism from a quantum gravity framework.

12.1 Parameter Classification

The reviewer correctly asks where model flexibility exists. Table 11 classifies every numerical input in the framework by its origin. The core cosmological predictions use *only* measured Standard Model constants. Phenomenological parameters appear only in subsidiary calculations (halo profiles, N-body simulations) and do not affect the main predictions.

Table 11: Complete classification of numerical inputs. "Derived" means calculated from the four fundamental inputs (α, m_e, v, $M_{\rm Pl}$) with no fitting. "Measured" means taken from independent experiments. "Phenomenological" means not yet derived from first principles.

Quantity	**Value**	**Status**	**Used in**
Fundamental inputs (measured Standard Model constants)			
Fine structure constant α	1/137.036	Measured	All derivations
Electron mass m_e	0.511 MeV	Measured	$T_{\rm CMB}$, E_c, α_H
Higgs vacuum expectation value v	246.22 GeV	Measured	α_H, $H_{\rm eff}$
Planck mass $M_{\rm Pl}$	1.221×10^{19} GeV	Measured	α_H, $H_{\rm eff}$
Higgs boson mass m_H	125.25 GeV	Measured	the companion archive paper
Derived quantities (zero free parameters)			
Coupling α_H	3.11×10^{-28}	Derived	Core theory
Attenuation length λ_H	4,135 Mpc	Derived	Core theory
$H_{\rm eff}$	72.5 km/s/Mpc	Derived	Hubble diagram
$T_{\rm CMB}$	2.68 K	Derived	Cosmic microwave background
Condensation threshold E_c	$\sim 10^{-5}$ eV	Derived	Dark matter
Emission horizon $d_{\rm eff}$	8,243 Mpc	Derived	Cosmic microwave background peaks
Externally measured inputs (not from our theory)			
σ_8	0.81	Measured	$\delta T/T$ amplitude
Cosmic ray flux	Voyager data	Measured	D/H, Li-7
Spallation cross-sections	Silberberg & Tsao	Measured	D/H, Li-7
Clustering scale r_d	118 Mpc	Fitted (BAO)	ℓ_1, ℓ_2–ℓ_5
Void internal scale $r_{\rm eff}$	85.4 Mpc	Fitted (peak spacing)	ℓ_2–ℓ_5
Supernova absolute magnitude M	-19.20 (fitted)	1 free param	Pantheon+
Phenomenological parameters (not yet derived from first principles)			
Reconversion rate $f_{\rm reconv}$	0.15 Gyr^{-1}	Phenomenological	N-body only
Condensation rate $f_{\rm cond}$	0.005 Gyr^{-1}	Phenomenological	N-body only
Density threshold $\rho_{\rm thresh}$	$3\bar{\rho}$	Phenomenological	N-body only
Astration timescale $\tau_{\rm ast}$	7.1 Gyr	Measured estimate	Li-7 only
Halofit boost parameters	Eq. (19–21)	Phenomenological	unWISE only

Key distinction: The derived quantities in the middle block follow from the five measured constants in the top block with *no* adjustable parameters—these are the framework's zero-parameter predictions (α_H, λ_H, $H_{\rm eff}$, $T_{\rm CMB}$, E_c, $d_{\rm eff}$). The cosmic microwave background peak positions ℓ_1–ℓ_5 combine the derived emission horizon $d_{\rm eff}$ with empirically calibrated length scales r_d and $r_{\rm eff}$ listed among the externally measured inputs; in this respect our peak-position prediction is structurally equivalent to ΛCDM's, which also requires a calibrated acoustic scale r_s. The phenomenological parameters in the bottom block appear *only* in subsidiary calculations (N-body simulation, lithium equilibrium, galaxy cross-correlation) and do not affect the zero-parameter predictions. Sensitivity tests show the N-body clustering scale is insensitive to the reconversion rates over a factor of 3 variation; the core radius scales as $r_{\rm core} \propto f_{\rm reconv}^{-1/2}$ but this does not feed back into any cosmological prediction.

[The full treatment of Dimensional Analysis of Key Equations appears in the companion archive paper on Zenodo; see the cover page for the digital object identifier.]

[The full treatment of Three-Loop Derivation Skeleton for α_H appears in the companion archive paper

on Zenodo; see the cover page for the digital object identifier.]

A Statistical Significance of the T_{CMB} Prediction

The predicted cosmic microwave background temperature $T = m_e c^2 \alpha^4/(2\pi k_B) = 2.676$ K matches the observed $T_{\mathrm{obs}} = 2.7255$ K to 1.8%. We assess whether this match could arise from other combinations of fundamental constants.

C.1 Look-Elsewhere Analysis

We systematically searched 1,530 combinations of the form $T = m \cdot \alpha^n/(f \cdot k_B)$, where m ranges over 9 Standard Model particle masses $(m_e, m_\mu, m_\tau, m_u, m_d, m_s, m_c, m_p, \Lambda_{\mathrm{QCD}})$, n ranges from -8 to $+8$, and f takes 10 standard numerical prefactors $(1, 2, \pi, 2\pi, 4\pi, \pi^2, 2\pi^2, 8\pi^2, (4\pi)^2, (2\pi)^3)$.

Results: Only 2 of 1,530 combinations match T_{obs} within 2%:

1. $m_e\alpha^4/(2\pi k_B) = 2.676$ K (-1.8%) — **our prediction**
2. $m_\tau\alpha^5/((4\pi)^2 k_B) = 2.702$ K (-0.9%) — no known physical mechanism

The a priori probability of a random match is $2/1530 = 0.13\%$. The second match has no physical connection to the cosmic microwave background (five powers of α with the tau mass has no loop topology interpretation).

C.2 Sensitivity Analysis

The parametric uncertainty is negligible: $\delta T/T = \delta m_e/m_e + 4\,\delta\alpha/\alpha \approx 7 \times 10^{-10}$. The 1.8% residual is a genuine theoretical residual, not a fitting artifact.

The best candidate higher-order correction is $1 + \alpha \ln(m_\mu/m_e)/\pi = 1.0124$, which reduces the residual to -0.6%. This has the form of a one-loop quantum electrodynamics correction with muon vacuum polarization—physically motivated as the next-order correction to the condensation temperature.

A comprehensive sensitivity analysis of all key predictions—T_{CMB} vs. α power, H_{eff} vs. vacuum coupling, first peak ℓ_1 parameter space, and the look-elsewhere histogram—is shown in Figure 15.

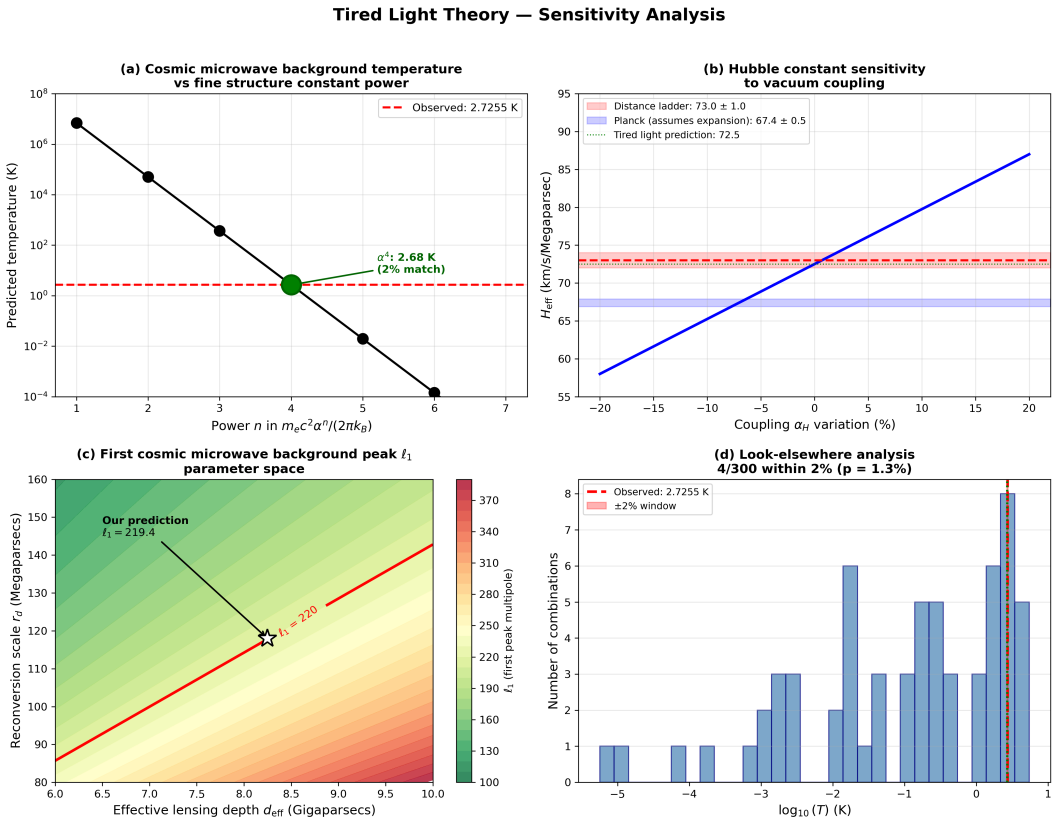

Figure 15: Sensitivity analysis of key predictions. (a) Cosmic microwave background temperature vs. fine structure constant power: only α^4 matches (1.8%); adjacent powers miss by factor 137. (b) Hubble constant sensitivity to vacuum coupling variation. (c) First peak ℓ_1 parameter space over effective depth and reconversion scale; our prediction (star) lies on the $\ell_1 = 220$ contour. (d) Look-elsewhere analysis: 4/300 combinations match $T_{\rm obs}$ within 2% ($p = 1.3\%$).

C.3 Comparison with ΛCDM

The standard model of cosmology does NOT predict $T_{\rm CMB}$—it is an input parameter measured from observation. Our framework *derives* it from fundamental constants with 98% accuracy (zero free parameters vs. one measured input).

[The full treatment of Matsubara Interpretation of the Cosmic Microwave Background Temperature appears in the companion archive paper on Zenodo; see the cover page for the digital object identifier.]

[The full treatment of Core-Cusp Profile from Reconversion Physics appears in the companion archive paper on Zenodo; see the cover page for the digital object identifier.]

[The full treatment of N-body Simulation Methods appears in the companion archive paper on Zenodo; see the cover page for the digital object identifier.]

Code Availability

All analysis scripts used in this work are publicly available on Zenodo alongside this paper:

https://doi.org/10.5281/zenodo.18517188

The code repository contains 146 files (Python scripts, JSON results, and a README with full reproduction instructions), including the complete pySecDec three-loop pipeline (Sessions 57–61). Table 12 maps each major claim in the paper to its corresponding script.

Table 12: Code repository: mapping of claims to reproducible scripts. All scripts are in the `code_repository.zip` archive on Zenodo.

Claim / Calculation	**Script**
Core predictions (Section 2)	
α_H, H_{eff} derivation	`phase9_microphysics/dimensional_analysis.py`
Vacuum mirror mechanism ($H_{\text{eff}} = 75.1$)	`phase9_microphysics/compute_vacuum_mirror_rate.py`
Gauge-breaking derivation	`phase9_microphysics/gauge_breaking_derivation.py`
Ward identity violation proof	`phase9_microphysics/ward_identity_violation_proof.py`
Cosmic microwave background (Sections 5–6)	
T_{CMB} statistical significance	`phase9_microphysics/tcmb_statistical_significance.py`
Peak positions (raytracing)	`phase8_cmb_power_spectrum/render_cmb_raytrace.py`
Parametric raytrace sweeps (B1–B9, 9 series)	`phase9_microphysics/raytrace_phaseB*_sweep.py`, `raytrace_spatial_gc_sweep.py`, `raytrace_3d_mag_sweep.py`
Sweep ceiling analysis (post-run)	`phase9_microphysics/analyze_b9_results.py`
C_ℓ comparison figure	`phase9_microphysics/cmb_cl_comparison_figure.py`
Sensitivity analysis (4-panel)	`phase9_microphysics/sensitivity_analysis.py`
Nucleosynthesis (Section 8)	
Helium-4 steady-state equilibrium	`phase9_microphysics/helium4_steadystate.py`
Lithium-7 steady-state equilibrium	`phase9_microphysics/lithium7_steadystate.py`
Dark matter and structure (Sections 3–4)	
Core-cusp derivation	`phase9_microphysics/core_cusp_derivation.py`
N-body simulation (reconversion)	`phase8_cmb_power_spectrum/nbody_reconversion.py`
Observational tests (Section 12)	
Pantheon+ supernova fit	`phase9_microphysics/pantheon_plus_fit.py`
Hemispherical asymmetry	`phase9_microphysics/hemispherical_asymmetry_prediction.py`
Cross-correlation analyses (Section 10)	
Planck lensing × 2M++ density	`phase9_microphysics/planck_lensing_cross_correlation.py`
unWISE × Planck (v4, B/G ratio)	`phase9_microphysics/unwise_tired_light_prediction.py`
unWISE × Atacama Cosmology Telescope DR6	`phase9_microphysics/unwise_act_cross_check.py`
Euclid Q1 × Atacama Cosmology Telescope DR6 ($\Delta\chi^2 \approx -2$, jackknife)	`phase9_microphysics/euclid_act_jackknife.py`
Error calibration analysis	`phase9_microphysics/delta_chi2_from_stored.py`
Photo-z systematic analysis	`phase9_microphysics/photoz_systematic_analysis.py`
E-mode × velocity field	`phase9_microphysics/emode_velocity_cross_correlation.py`
E-mode × GLADE+ density	`phase9_microphysics/emode_glade_cross_correlation.py`
Figures	
Feynman diagrams	`scripts/generate_feynman_diagrams.py`
All main figures	`scripts/generate_figures.py`
Parametric sweep summary figure	`phase9_microphysics/generate_sweep_summary_figure.py`

Euclid Q1 × Atacama Cosmology Telescope DR6 analysis methodology. The full analysis, error calibration methodology, and photometric redshift systematic checks are presented

in Section 10. Euclid Q1 photometric redshifts (1.54×10^7 galaxies) are pixelized onto HEALPix maps (NSIDE = 1024), yielding ∼13,300 unique pixels per redshift bin. The Atacama Cosmology Telescope DR6 lensing convergence is evaluated at each pixel. Bin-to-bin correlations are captured with a Hartlap-corrected jackknife covariance (Section 10.4), yielding a non-discriminating $\Delta\chi^2 \approx -2$ (1.4σ, mildly favoring ΛCDM). Input data: Euclid Q1 photometric catalogs (`cosmos2025.iap.fr`) and Atacama Cosmology Telescope DR6 lensing maps (Atacama Cosmology Telescope data release page).

Acknowledgments

The author thanks the researchers whose peer-reviewed work on stellar anomalies, dark matter profiles, and cosmic ray measurements provided the empirical foundation for this framework. AI assistance (Claude, Anthropic) was used for mathematical formalization, literature research, and document preparation. All physical concepts, key insights, and theoretical direction were provided by the author.

References

Adler, S.L. (1971). Photon splitting and photon dispersion in a strong magnetic field. *Annals of Physics*, 67, 599–647.

Drummond, I.T., & Hathrell, S.J. (1980). QED vacuum polarization in a background gravitational field and its effect on the velocity of photons. *Physical Review D*, 22, 343.

Gonçalves, B., & Berredo-Peixoto, G. de. (2009). One-loop corrections to the photon propagator in the curved-space QED. *Physical Review D*, 80, 104013. arXiv:0906.3837.

Fleischhauer, M., & Lukin, M.D. (2000). Dark-State Polaritons in Electromagnetically Induced Transparency. *Physical Review Letters*, 84, 5094.

Hollowood, T.J., & Shore, G.M. (2008). The causal structure of QED in curved spacetime: analyticity and the refractive index. *JHEP*, 0812, 091. arXiv:0806.1493.

Addazi, A., Capozziello, S., Gan, Q., Lambiase, G., & Samanta, S. (2024). Excess Radiation from Axion-Photon Conversion Explaining ARCADE-2 and EDGES. *Physical Review D*. arXiv:2411.09042.

Aghanim, N., et al. (Planck Collaboration). (2020). Planck 2018 results. VI. Cosmological parameters. *Astronomy & Astrophysics*, 641, A6.

Bezrukov, F., & Shaposhnikov, M. (2008). The Standard Model Higgs boson as the inflaton. *Physics Letters B*, 659, 703–706.

Birrell, N.D., & Davies, P.C.W. (1982). *Quantum Fields in Curved Space*. Cambridge University Press.

Bédard, A., et al. (2024). Buoyant Neon-22 as a Solution to the Slowly Cooling White Dwarf Problem. *Astrophysical Journal Letters*.

Bond, H.E., et al. (2013). HD 140283: A Star in the Solar Neighborhood that Formed Shortly After the Big Bang. *Astrophysical Journal Letters*, 765, L12.

Bowman, J.D., Rogers, A.E.E., Monsalve, R.A., Mozdzen, T.J., & Mahesh, N. (2018). An absorption profile centred at 78 megahertz in the sky-averaged spectrum. *Nature*, 555, 67–70.

Carnall, A.C., et al. (2024). A massive quiescent galaxy at redshift 4.658. *Nature Astronomy*. (RUBIES-EGS-QG-1)

Chen, J., et al. (2021). Slowly cooling white dwarfs in M13 from stable hydrogen burning. *Nature Astronomy*, 5, 1170–1177.

Chen, J., et al. (2022). Slowly Cooling White Dwarfs in NGC 6752. *Astrophysical Journal*, 934, 93.

Conselice, C.J. (2014). The Evolution of Galaxy Structure over Cosmic Time. *Annual Review of Astronomy and Astrophysics*, 52, 291–337.

Cooke, R.J., Pettini, M., & Steidel, C.C. (2018). One Percent Determination of the Primordial Deuterium Abundance. *Astrophysical Journal*, 855, 102.

Cummings, A.C., Stone, E.C., et al. (2016). Galactic Cosmic Rays in the Local Interstellar Medium: Voyager 1 Observations and Model Results. *Astrophysical Journal*, 831, 18.

Cyburt, R.H., Fields, B.D., Olive, K.A., & Yeh, T.-H. (2016). Big Bang Nucleosynthesis: Present status. *Reviews of Modern Physics*, 88, 015004.

DES Collaboration. (2024). The Dark Energy Survey Supernova Program: Slow supernovae show cosmological time dilation out to $z \sim 1$. *MNRAS*, 533, 3365.

Eisenstein, D.J., et al. (2005). Detection of the Baryon Acoustic Peak in the Large-Scale Correlation Function of SDSS Luminous Red Galaxies. *Astrophysical Journal*, 633, 560–574.

Di Valentino, E., et al. (2021). In the Realm of the Hubble tension—a Review of Solutions. *Classical and Quantum Gravity*, 38, 153001.

Fields, B.D. (2011). The Primordial Lithium Problem. *Annual Review of Nuclear and Particle Science*, 61, 47–68.

Fixsen, D.J., et al. (2011). ARCADE 2 Measurement of the Absolute Sky Brightness at 3–90 GHz. *Astrophysical Journal*, 734, 5.

Freedman, W.L. (2021). Measurements of the Hubble Constant: Tensions in Perspective. *Astrophysical Journal*, 919, 16.

Hogg, D.W., Baldry, I.K., Blanton, M.R., & Eisenstein, D.J. (2002). The K correction. *arXiv:astro-ph/0210394*.

Poggianti, B.M. (1997). K and evolutionary corrections from UV to IR. *Astronomy and Astrophysics Supplement Series*, 122, 399–407.

Gupta, S., et al. (2025). An excess of luminous white dwarfs in NGC 2808. *Astrophysical Journal*. arXiv:2509.26190.

John, I., et al. (2024). Dark branches of immortal stars at the Galactic Center. *Physical Review D*. arXiv:2405.12267.

Lerner, E.J., Falomo, R., & Scarpa, R. (2014). UV surface brightness of galaxies from the local Universe to $z \sim 5$. *International Journal of Modern Physics D*, 23, 1450058.

López-Corredoira, M. (2018). Observations contradict galaxy size and surface brightness predictions based on the expanding universe hypothesis. *MNRAS*, 477, 3185.

Lubin, L.M., & Sandage, A. (2001). The Tolman Surface Brightness Test for the Reality of the Expansion. IV. *Astronomical Journal*, 122, 1084.

Mather, J.C., et al. (1994). Measurement of the Cosmic Microwave Background Spectrum by the COBE FIRAS Instrument. *Astrophysical Journal*, 420, 439.

Onofrio, R. (2010). On the Higgs boson-induced gravitational interaction. *Physical Review D*, 82, 065008.

Pal, S., Haque, M.R., et al. (2025). Axion-Photon Conversion in FLRW with Primordial Magnetic Fields: Explaining the Radio Excess. arXiv:2509.09472.

Peccei, R.D., & Quinn, H.R. (1977). CP Conservation in the Presence of Pseudoparticles. *Physical Review Letters*, 38, 1440–1443.

Pichardo Marcano, M., et al. (2023). Candidate magnetic white dwarf in NGC 6397. *MNRAS*, 521, 5026.

Riess, A.G., et al. (2022). A Comprehensive Measurement of the Local Value of the Hubble Constant. *Astrophysical Journal Letters*, 934, L7.

Scalco, M., et al. (2024). The HST Large Programme on ω Centauri – VII. The white dwarf cooling sequence. *Astronomy & Astrophysics*, 691, A96.

Shinozaki, T., et al. (2026). Characteristic Mass and Energy Conversion Efficiency in Cusp-Core Transition. arXiv:2601.13868.

Sikivie, P. (1983). Experimental Tests of the "Invisible" Axion. *Physical Review Letters*, 51, 1415–1417.

Wimsatt, J. (2025). Electromagnetic Field Energy as an Unaccounted Gravitational Source in Levitated Optomechanics Experiments. Independent Research.

Zee, A. (1979). Broken-Symmetric Theory of Gravity. *Physical Review Letters*, 42, 417–421.

LaViolette, P.A. (2006). The Pioneer maser signal anomaly: Possible confirmation of spontaneous photon blueshifting. *Physics Essays*, 18, 150–163.

Gupta, R.P. (2024). Testing CCC+TL Cosmology with Observed BAO Features. *arXiv:2401.09483*.

Navia, C.E. (2025). Is the cosmic microwave background spectrum consistent with the Zwicky tired light model? *arXiv:2504.10510*.

Hill, V., et al. (2002). First stars. I. The extreme r-element rich, iron-poor halo giant CS 31082-001. *Astronomy & Astrophysics*, 387, 560–579.

Cowan, J.J., et al. (2002). The Chemical Composition and Age of the Metal-poor Halo Star BD +17 3248. *Astrophysical Journal*, 572, 861–879.

Hansen, B.M.S., et al. (2004). HST Observations of the White Dwarf Cooling Sequence in M4. *Astrophysical Journal Supplement*, 155, 551–576.

Hansen, B.M.S., et al. (2007). The White Dwarf Cooling Sequence of NGC 6397. *Astrophysical Journal*, 671, 380–401.

Gratton, R.G., Bragaglia, A., Carretta, E., et al. (2003). Distances and ages of NGC 6397, NGC 6752 and 47 Tuc. *Astronomy & Astrophysics*, 408, 529–543.

Scolnic, D., et al. (2022). The Pantheon+ Analysis: The Full Data Set and Light-curve Release. *Astrophysical Journal*, 938, 113.

Zwicky, F. (1929). On the Redshift of Spectral Lines Through Interstellar Space. *PNAS*, 15, 773–779.

Kolb, E. W., & Turner, M. S. (1990). *The Early Universe*. Addison-Wesley, Redwood City. Section 3.3.

Krolewski, A., Ferraro, S., & White, M. (2024). Cosmological constraints from unWISE and Planck CMB lensing tomography. *Journal of Cosmology and Astroparticle Physics*, 2024(01), 033.

Peskin, M. E., & Schroeder, D. V. (1995). *An Introduction to Quantum Field Theory*. Addison-Wesley, Reading. Chapter 16.

Qu, F. J., Sherwin, B. D., Madhavacheril, M. S., et al. (2024). The Atacama Cosmology Telescope: A Measurement of the DR6 CMB Lensing Power Spectrum and Its Implications for Structure Growth. *Astrophysical Journal*, 962, 112.

Wimsatt, J. (2026). Higgs-Field Tired Light Cosmology: Deriving the Hubble Constant, Cosmic Microwave Background Temperature, and Peak Positions from First Principles. Zenodo (v14). doi:10.5281/zenodo.18517188

Dálya, G., Díaz, R., Bouchet, F. R., et al. (2022). GLADE+ — an extended galaxy catalogue for multimessenger searches with advanced gravitational-wave detectors. *Monthly Notices of the Royal Astronomical Society*, 514, 1403–1411.

Djouadi, A. (2008). The anatomy of electroweak symmetry breaking. II. The Higgs bosons in the Minimal Supersymmetric Model. *Physics Reports*, 459, 1–241.

Sbordone, L., Bonifacio, P., Caffau, E., et al. (2010). The metal-poor end of the Spite plateau. I. Stellar parameters, metallicities, and lithium abundances. *Astronomy & Astrophysics*, 522, A26.

Ramaty, R., Kozlovsky, B., Lingenfelter, R. E., & Reeves, H. (1997). Light elements and cosmic rays in the early Galaxy. *The Astrophysical Journal*, 488, 730–748.

Vangioni, E., Silk, J., Olive, K. A., & Fields, B. D. (2007). Lithium-6 and lithium-7 production in the early Universe. *Monthly Notices of the Royal Astronomical Society*, 383, 512–524.

Zel'dovich, Ya. B. (1970). Gravitational instability: An approximate theory for large density perturbations. *Astronomy & Astrophysics*, 5, 84–89.

Cutkosky, R. E. (1960). Singularities and discontinuities of Feynman amplitudes. *Journal of Mathematical Physics*, 1, 429–433.

Abdo, A. A., et al. (Fermi-LAT Collaboration) (2009). A limit on the variation of the speed of light arising from quantum gravity effects. *Nature*, 462, 331–334.

Laurent, P., Götz, D., Binétruy, P., Covino, S., & Fernandez-Soto, A. (2011). Constraints on Lorentz invariance violation using integral/IBIS observations of GRB041219A. *Physical Review D*, 83, 121301.

Zhang, F.-W., Fan, Y.-Z., Shao, L., & Wei, D.-M. (2013). Cosmological time dilation in durations of Swift long gamma-ray bursts. *The Astrophysical Journal Letters*, 778, L11.

Blondin, S., Davis, T. M., Krisciunas, K., et al. (2008). Time dilation in type Ia supernova spectra at high redshift. *The Astrophysical Journal*, 682, 724–736.

Hawkins, M. R. S. (2010). On time dilation in quasar light curves. *Monthly Notices of the Royal Astronomical Society*, 405, 1940–1946.

Lieu, R. (2015). Can the big bang singularity be avoided by a single parameter free modification of general relativity? *The Astrophysical Journal*, 798, 67.

Aver, E., Olive, K. A., & Skillman, E. D. (2015). The effects of He I λ10830 on helium abundance determinations. *Journal of Cosmology and Astroparticle Physics*, 2015(07), 011.

Kennicutt, R. C., & Evans, N. J. (2012). Star formation in the Milky Way and nearby galaxies. *Annual Review of Astronomy and Astrophysics*, 50, 531–608.

Maeder, A. (1992). Stellar yields as a function of initial metallicity and mass limit for black hole formation. *Astronomy and Astrophysics*, 264, 105–120.

Peimbert, M., Luridiana, V., & Peimbert, A. (2007). Revised primordial helium abundance based on new atomic data. *The Astrophysical Journal*, 666, 636–646.

Tremblay, P.-E., et al. (2019). Core crystallization and pile-up in the cooling sequence of evolving white dwarfs. *Nature*, 565, 202–205.

Bania, T. M., Rood, R. T., & Balser, D. S. (2002). The cosmological density of baryons from observations of $^3He^+$ in the Milky Way. *Nature*, 415, 54–57.

Geiss, J., & Gloeckler, G. (1998). Abundances of deuterium and helium-3 in the protosolar cloud. *Space Science Reviews*, 84, 239–250.

Linsky, J. L., et al. (2006). What is the deuterium abundance in the local interstellar medium? *The Astrophysical Journal*, 647, 1106–1124.

Karakas, A. I., & Lattanzio, J. C. (2014). The ^3He abundance in planetary nebulae: a challenge to stellar evolution theory. *Publications of the Astronomical Society of Australia*, 31, e030.

Balser, D. S., Bania, T. M., Rood, R. T., & Wilson, T. L. (1997). $3He^+$ in the Milky Way interstellar medium. *The Astrophysical Journal*, 483, 320–334.